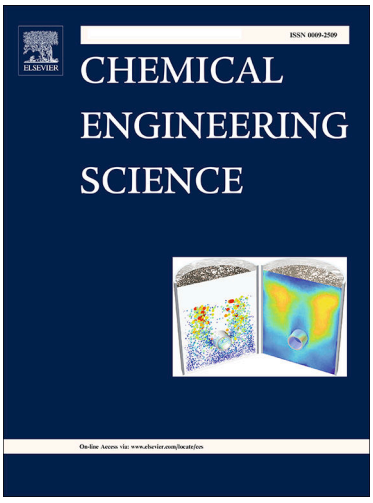

Dynamic X-ray tomography of microfibrous cellulose liquid foams using deep learning

Syeda Rubaiya Muin, Patrick T. Spicer, Kunning Tang, Yufu Niu, Seyedeh Maryam Hosseini, Peyman Mostaghimi, Ryan T. Armstrong

PII: S0009-2509(21)00738-7
DOI: https://doi.org/10.1016/j.ces.2021.117173
Reference: CES 117173

To appear in: *Chemical Engineering Science*

Received Date: 9 July 2021
Accepted Date: 2 October 2021

Please cite this article as: S. Rubaiya Muin, P.T. Spicer, K. Tang, Y. Niu, S. Maryam Hosseini, P. Mostaghimi, R.T. Armstrong, Dynamic X-ray tomography of microfibrous cellulose liquid foams using deep learning, *Chemical Engineering Science* (2021), doi: https://doi.org/10.1016/j.ces.2021.117173

Dynamic X-ray tomography of microfibrous cellulose liquid foams using deep learning

Syeda Rubaiya Muin[1], Patrick T. Spicer[2], Kunning Tang[1], Yufu Niu[1], Seyedeh Maryam Hosseini[2], Peyman Mostaghimi[1], Ryan T. Armstrong[1]

[1] School of Minerals and Energy Resources Engineering, University of New South Wales, Sydney, Australia

[2] School of Chemical Engineering, University of New South Wales, Sydney, Australia

Abstract:

Using X-ray microcomputed tomography (micro-CT) as a 3D microstructural analysis tool elucidates the time evolution of foam Plateau borders and nodes, providing unprecedented vision of foam dynamics. Deep learning facilitates the capability by allowing for quantifiable images to be collected at the time scale of five minutes. The stability mechanism of microfibrous cellulose is assessed demonstrating that trapping of fibers in the foam structure results in a critical concentration that marks an arrested foam. The mechanism of arrest is explained by 3D structural information extracted from micro-CT and confocal laser scanning microscopy images demonstrating the entanglement of cellulose fibers. A detailed analysis of the micro-CT data is provided to substantiate the quantitative nature of the digital images and assess advanced deep learning approaches. It is demonstrated that deep learning allows for the dynamic imaging of liquid foams whereas traditional data processing approaches cannot capture accurate geometrical information of foam structure.

Keywords:

Liquid foams, Dynamic micro-CT, Image segmentation, Convolutional neural network (CNN), Deep-learning, Microfibrous cellulose nanofibers (MFC)

1. Introduction

Laboratory-based microcomputed tomography (micro-CT) is a powerful technique to visualize porous systems in 3D with high spatial resolution on the order of a few micrometres (Bultreys et al., 2016; Di Michiel et al., 2005). Bench-top micro-CT systems provide a non-invasive, relatively affordable tool to investigate how the 3D internal structure of a material evolves under different external conditions. As such, micro-CT is becoming an indispensable technique for the study of porous materials that significantly impact a wide range of industries, such as petroleum (Cnudde and Boone, 2013; Wildenschild and Sheppard, 2013), mining (Wang and Miller, 2020), food sciences

(Schoeman et al., 2016) and the medical industry (Ritman, 2011; Swain and Xue, 2009). Nevertheless, image acquisition times for bench-top micro-CT systems are sufficiently high, on the order of minutes to hours (Bultreys et al., 2016), which makes it challenging to study short-lived, fast-aging dynamic systems, such as liquid foams that may not sustain or remain static during relatively long scan times.

The stability of liquid foams is of paramount interest to a wide range of engineering applications, such as enhanced oil recovery (Rossen, 2017), mineral processing (Matis and Mavros, 1991), personal care products (Arzhavitina and Steckel, 2010), and food and beverage manufacturing (Dickinson, 2010). Traditionally, foam stability is evaluated via observing the bulk foam structure from the top or side of a glass column, which can be inaccurate due to wall effects (Cheng and Lemlich, 1983; Papara et al., 2009) and provides only a limited view of the foam structure. Whereas how the 3D foam structure evolves over time is important for the understanding of the aging dynamics, which plays a pivotal role in determining product performance and process efficiency (Farrokhpay, 2011; Gonzenbach et al., 2006; Rossen, 2017).

Foams are intrinsically unstable systems that undergo destabilization via three main mechanisms: (1) coalescence (Cho and Laskowski, 2002; Langevin, 2015), (2) inter-bubble gas diffusion (also known as diffusive coarsening or Ostwald ripening) (Gandolfo and Rosano, 1997; Stevenson, 2010), and (3) gravity drainage (Kruglyakov et al., 2008; Verbist et al., 1996). Specifically, it is vital to study foam drainage as both coalescence and diffusive coarsening processes rely on the film thickness, which is determined by the drainage rate (Bhakta and Ruckenstein, 1997; Weaire and Hutzler, 2001). Thinner films are easier to rupture, therefore, easier to coalesce (Briceño-Ahumada et al., 2016; Carrier and Colin, 2003). On the other hand, inter-bubble gas diffusion is faster via thinner liquid films (Hilgenfeldt et al., 2001; Hutzler and Weaire, 2000). Conventionally, foam drainage is studied in two dimensions using various techniques, such as the pressure drop technique (Exerowa and Kruglyakov, 1997), forced drainage method (Weaire and Hutzler, 2001), free drainage technique (Koehler et al., 2000; Stone et al., 2002), or using the Plateau border apparatus (Pitois et al., 2005). However, these experimental techniques do not provide information on how the 3D structure of the foam evolves during the drainage process. Hence, a detailed understanding of foam drainage in 3D is crucial for accurate modelling and simulations of foam aging mechanisms that determine its stability.

Foam drainage can be slowed down via addition of rheological resistance to the liquid phase. Addition of nano-particles (Arriaga et al., 2012; Hunter et al., 2009; Stocco et al., 2011a), polymers (Alargova et al., 2004; Bureiko et al., 2015), food proteins (Damodaran, 2005; Graetz et al., 2020; Hailing and Walstra, 1981), and viscous liquids, such as glycerol (Briceño-Ahumada et al., 2016; Muin

et al., 2020) are common ways of achieving foam stabilization via increasing the bulk viscosity of the liquid phase. However, a major disadvantage with these methods is the high concentration of particles required to achieve stabilization, which can be costly, and cause a nuisance during manufacturing processes (Lam et al., 2014).

The study of microfibrous cellulose (MFC) liquid foams can be advantageous as it has scope for progress in a wide range of applications. Aqueous MFC is a non-Newtonian fluid that consists of cellulose microfibers that can impart a yield stress while retaining a relatively low viscosity (Solomon and Spicer, 2010). MFC sourced from bacteria is pure cellulose, whereas plant-based MFC is a mixture of lignocellulose and cellulose, and has attracted various patents (Charreau et al., 2013) for use in the food industry, and the paper and pulp industry due to its non-toxic, biodegradable, and strong mechanical properties (Kontturi et al., 2018; Lavoine and Bergström, 2017). However, to the best of our knowledge, there are only two studies that focuses on how cellulose microfibers influence the bulk stability of liquid foams (Cervin et al., 2015; Xiang et al., 2019b). The results from these studies highlight that the high aspect ratio of the MFC contributes to its exceptional foam stability on the order of days. However, a detailed microscopic analysis of the foam aging mechanisms that contributed to the exceptional stability was not conducted.

Laboratory micro-CT systems are traditionally an uncommon choice for scanning fast aging foams due to the requirement that samples remain static during the scan time (Barrett and Keat, 2004; Boas and Fleischmann, 2012). Due to this limitation, micro-CT has only been previously used to study liquid foams using synchrotron sources (García-Moreno et al., 2017; Lambert et al., 2005) that provide fast acquisition times, ultra-stable foams made up of relatively inert gases (Meagher et al., 2011) or nano-particle stabilized foams (Stocco et al., 2011a), which do not undergo drainage during the scan time. Synchrotron X-ray sources are limited in number and involve exceptionally high operational costs in comparison to benchtop systems, which are much more accessible. The scan times of benchtop systems can be tuned to reduce movement artifacts; however, if the scan time is too short, it can lead to a low signal-to-noise ratio (SNR) (Bultreys et al., 2016). Ultimately the SNR determines the image quality and the extent to which quantitative data can be extracted from the images. So, the challenge is to develop an approach using micro-CT that can provide high enough quality images of dynamically aging foams such that relevant foam aging metrics can be extracted from the digital images. Thus, MFC is chosen for this foam study as it has fast dynamics in comparison to traditional particle-stabilized foams and is a good example of a sustainable material that is relatively less viscous but can still stabilize a foam.

To address this challenge, we propose the use of convolutional neural networks (CNNs) built within a deep learning platform (Da Wang et al., 2020; Jiang et al., 2018; Niu et al., 2020; Shelhamer et al., 2017; Tamada et al., 2020; Wang et al., 2021; Xiang et al., 2019a) to employ accurate segmentation of dynamic foam images that have a low SNR. The CNNs investigated in this study rely on supervised learning from ground truth (GT) data to accurately identify the pixel distributions at the air-liquid interfaces. With this effort, the utility of bench-top micro-CT systems can be enhanced despite its known limitations regarding image quality and scanning time. Overall, this study presents a novel approach to study dynamic MFC foams using laboratory micro-CT systems and CNNs to enable accurate image segmentation and extraction of geometrical metrics relevant to foam aging that are inaccessible with traditional techniques.

2. Methods and materials

Figure 1 illustrates the experimental workflow undertaken to characterize the dynamics of liquid MFC foams. Firstly, a preliminary bulk foam study at MFC concentrations 0.025% and 0.05% was carried out to observe how the foam evolves after generation to determine suitable aging times. Next, fast 5-minute scans were imaged at selected aging times (t) using a standard bench-top micro-CT system. However, since these images had low SNR, segmentation was carried out to test the applicability of current machine learning approaches. Finally, the segmented binary foam images for the two MFC concentrations were analysed to gain an in-depth understanding of the stabilization mechanism of MFC.

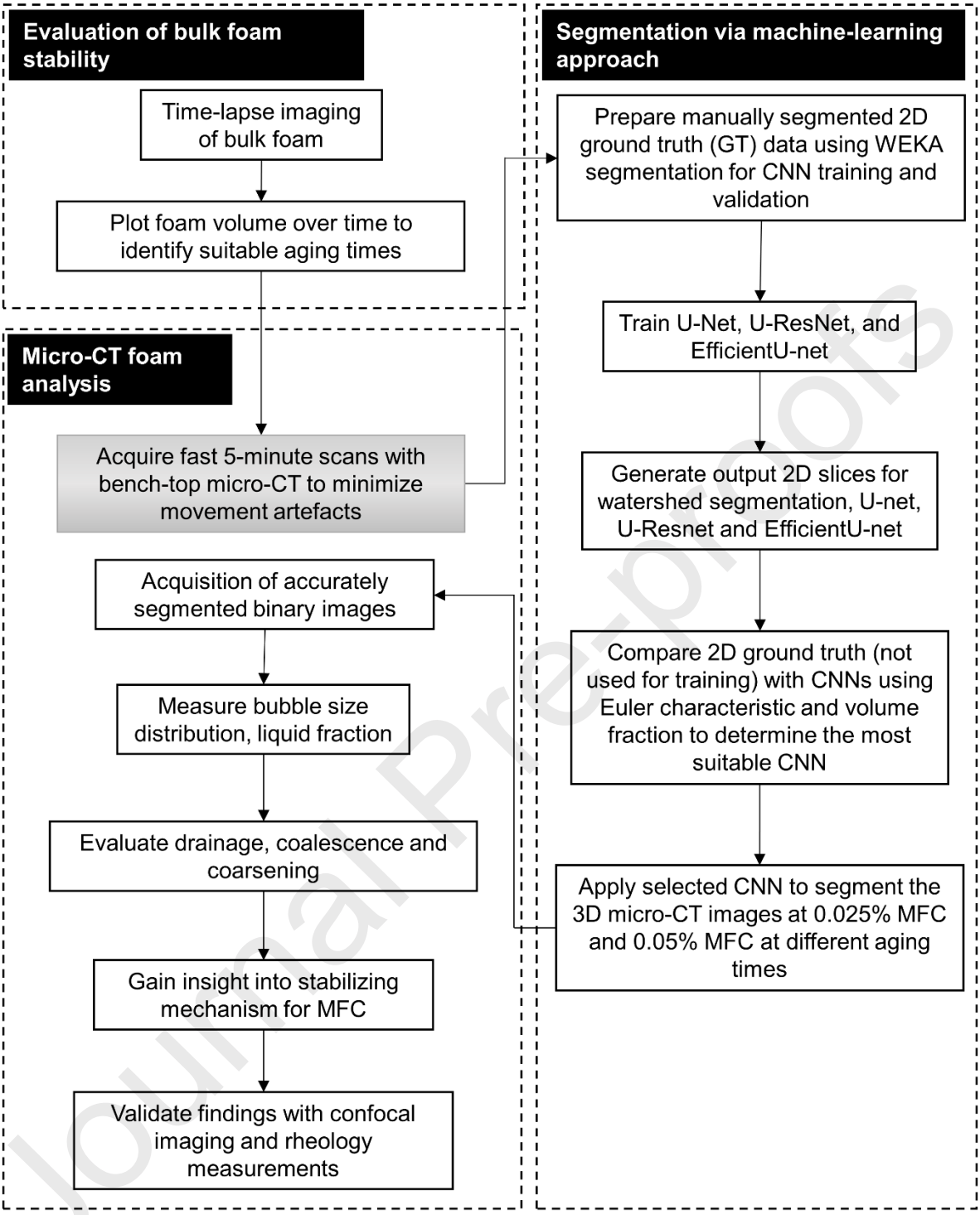

Figure 1: Experimental workflow for evaluating the foam dynamics of fast-draining liquid foams using a benchtop micro-CT system. The short 5-minute micro-CT scans were segmented via a machine-learning approach to minimize errors due to low SNR. The output binary images were then analyzed to evaluate the foam dynamics for MFC concentrations 0.025% and 0.05% and gain insight into the stabilizing mechanism of MFC.

2.1 Evaluation of bulk foam stability

The bulk foam stability was assessed for MFC concentrations of 0.025% and 0.05% by weight. These concentrations were considered suitable as the MFC foams become bubbly liquids (i.e. $\phi > 0.36$) at concentrations close to 0.1% (Saint-Jalmes, 2006). This is due to the high water retention ability of MFC (Nakagaito et al., 2009) and the significant yield stress of MFC at these relatively low concentrations (Song et al., 2019a). The MFC foams were prepared using 6 g/L Sodium dodecyl sulfate (SDS), 1:6 m/m% Sodium iodide, and 0.85 g/L Octan-1-ol purchased from Sigma Aldrich, and desired concentration of microfibrous cellulose (MFC) dispersion. The stock MFC dispersion was prepared by first rinsing the bacterial cellulose samples (Wong Coco, Indonesia) with deionized water, and then coarse blending using a laboratory blender (Sunbeam, Australia). Next, the blended sample was homogenized for 5 minutes using a T18 digital Ultra Turrax homogenizer, IKA, and 0.5 ml of Kathon (Supelco, USA) preservative was added to approximately 0.4% cellulose to prepare the stock MFC dispersion. This procedure is similar to Song et al. (2019a, 2019b). Finally, deionized water was added to achieve the desired MFC concentrations in the foam solution.

Initially, SDS and NaI salt were mixed with deionized water and sonicated for 15 minutes to allow all solids to dissolve. Next, Octan-1-ol and MFC in the required proportions were pipetted into the surfactant-salt solution. The resulting solution was mixed with a Ratek vortex mixer set at 2500 RPM for 1 minute to prepare a homogenous foam solution. Finally, the foams were prepared using the Bartsch method (Bartsch, 1924) by constantly shaking the samples for 1 minute.

Three replicates were prepared for the two concentrations of MFC foams and closely monitored using a high-resolution camera (Moticam 10MP, Motic) by capturing one frame per 3.5 minutes over 100 hours. The time-lapse images were then imported to Fiji software (Schindelin et al., 2012) to measure the foam volume (V_f) over time to evaluate stability. The bubbly liquid zone and foam zone are difficult to distinguish using standard thresholding. Thus, WEKA segmentation (Arganda-Carreras et al., 2017) was used for more accurate identification of the foam area, which was then used to calculate the foam volume for the time-lapse images.

2.2 Acquisition of dynamic micro-CT images

The bench-top Heliscan micro-CT equipment at the University of New South Wales Tyree X-ray imaging facility was used to collect time-lapsed images of the foam dynamics. The micro-CT system consists of a Phoenix Nanofocus tube with a diamond window and a high-quality flatbed detector (3072x 3072 pixels, 3.75 fps readout rate). Identical preparation method as Section 2.1 was used to prepare the foam samples, and sequential micro-CT images were collected using 5-minute scan

times with a lag time of 1 minute between imaging, i.e. temporal resolution of 6 minutes. Multiple images with a spatial resolution of 5.5 µm were collected at early and late aging times for both 0.025% and 0.05% MFC foams. Each scan was obtained using a circular trajectory with the scan parameters specified in Table 1.

Table 1: Scan parameters used for dynamic micro-CT imaging

Description	Scan parameters
Voxel size (µm)	5.55
Filter used	1 mm Aluminium
Voltage (kV)	80
Current (µA)	82
Exposure time (s)	0.43
Number of accumulations	1
Scan duration (minutes)	5
Number of projections	800
Sample position for imaging	~2 mm above foam-liquid interface
Height of image (mm)	6.98

2.3 Segmentation via machine-learning approach

To ensure accurate segmentation of the dynamic foam images, we firstly determine the best performing CNN for this task by comparing commonly used network architectures, such as U-Net, U-Resnet, and EfficientU-net. CNNs depend on supervised learning, which means that the architectures need to be trained using data. Due to the lack of actual foam ground truth (GT) data, we created GT data using a manual segmentation method that provides identification of the respective phases yet

remains impractical to implement for an entire 3D image; the details are provided in the next section.

To determine which network is performing well and whether it performs better than traditional segmentation, quantitative analyses were carried out using three 2D GT slices of 1000x1000 pixels to compare the Euler characteristic (χ) of the connected liquid phase, total bubble area (A_g), and total liquid film area (A_l). The χ indicates connectivity (Michielsen and De Raedt, 2001; Ohser and Mücklich, 2000) and is calculated as

$$\chi = \text{objects} - \text{loops} + \text{cavities}. \quad (1)$$

For measuring χ of the liquid foam phase, the number of *objects* is always one and there are physically no *cavities*, and the number of redundant *loops* consist of the number of unique complete paths that can be formed around the air phase.

In addition to the bulk analyses, a region-based accuracy was also determined to assess where the foam interfaces are segmented correctly. To do this, the binary outputs generated from the CNN were subtracted from the GT data to determine the misclassified regions. These subtracted output images were then multiplied by the Euclidean distance map of the GT data, which assigns a distance value to each voxel in the image based on its distance from an interface. Then the frequency distribution of misaligned voxels with respect to distance from the nearest interfaces was determined in 2D. This is performed since interface regions are often the most difficult to segment, and thus a defining feature of any given segmentation approach would be how well the interfaces are resolved (Sheppard et al., 2004). This is particularly important for the study of foam systems, where interfacial forces play a dominant role in the dynamics (Pugh, 1996).

2.3.1 Preparation of manually segmented GT data

Two sets of GT images were prepared for (1) training and (2) validation. For the manual segmentation, interfaces were manually fed into the WEKA classification tool (Arganda-Carreras et al., 2017) to minimize unavoidable human errors in the manual segmentation. All the interfaces were manually drawn and fed into the classifier for generating highly accurate GT slices. The pixels in the image were then manually selected to remove any wrongly identified phases. While the approach does introduce human bias, the overall quality of the segmented images can be seen in Figure 2. As observed in Figure 2, the interfaces are well resolved and representative of the foam system.

For training data, greyscale 2D slices with the least movement, i.e., less blurry or fewer double-edges, were cropped and manually segmented using WEKA segmentation. This was done to minimize errors due to poor user judgment in generating the manual GT data. The GT slices used for training were of non-uniform sizes but comprised of a total area of 5.4x 10^6 pixels.

For the validation data, a total area of 3x10^6 pixels, i.e., three 2D slices of 1000x1000 pixels, were selected from three vertical elevations: top, middle, and bottom, as the drainage dynamics and the extent of motion artifacts are likely to vary with elevation for the 3D image. Therefore, using three different heights allows us to evaluate the performance over the entire range of possible image quality, and thus evaluate how well the CNNs perform across the entire 3D dataset.

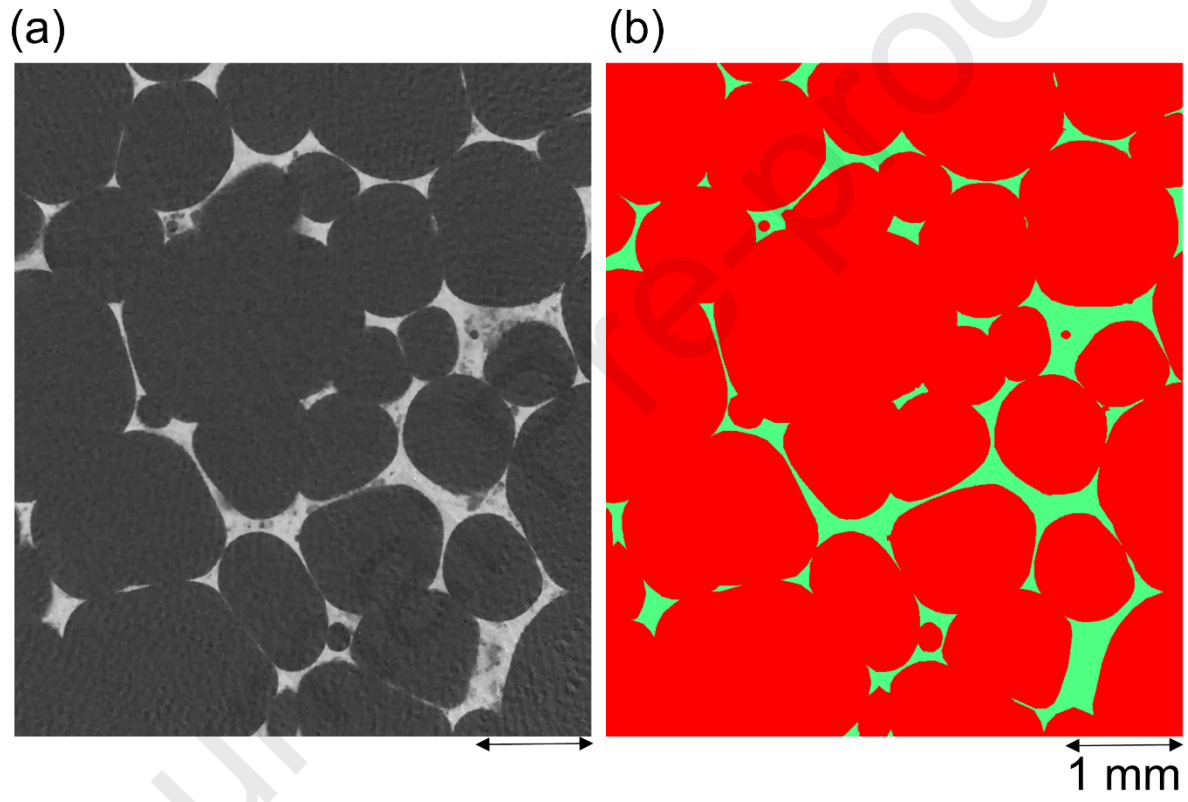

Figure 2: Generation of synthetic GT data via WEKA segmentation of a noisy 5-minute foam scan. An increasingly high number of interfaces were manually fed into the WEKA classifier to enhance accuracy of the manual segmentation.

2.3.2 Traditional segmentation with non-local means and watershed

Three 2D slices were also processed using a non-local means (NLM) filter (Buades et al., 2005) followed by watershed segmentation (Vincent and Soille, 1991) in Avizo™ to provide a baseline comparison to the CNN-generated data. This traditional method was specifically chosen as it provides the highest visual accuracy compared to other filtering steps and thresholding methods

available in the Avizo™ software for the given dataset. Generally, the NLM filter is effective for denoising a wide range of image noise common for X-ray micro-CT techniques (Buades et al., 2011; Manjón et al., 2008; Sarker et al., 2012), while watershed segmentation is advantageous as it provides relatively fast, accurate boundary results with minimal user interference (Schlüter et al., 2014).

2.3.3 Training schedule

The training dataset was cropped into 1180 sub-slices of 96x96 pixels. The slices were split into 960 for training and 240 for testing. Validation was then performed using 2D GT to compare the resulting geometrical measures of the resulting foam structure. The batch size was set to be 16 image slices. All networks were trained for 200 epochs with an initial learning rate of 0.00001, which is halved if the accuracy is not improved in 80 epochs. Adam solver was selected as the optimizer and cross-entropy loss was used as the loss function

$$cross\ entropy\ loss = -\sum_{k=1}^{X} (p_k log q_k),$$

where *p* is the GT target in scalar, *q* is the prediction output after softmax function, and *X* is the number of labels. The training was implemented in PyTorch, using a Nvidia RTX 3090 Graphic Processing unit.

2.3.4 U-Net segmentation

U-Net (Ronneberger et al., 2015) has a symmetric encoding-decoding structure that is widely used for image-to-image translation. The long skip connection in U-Net is utilized to link the encoding layers to their corresponding decoding layers by concatenation, which is beneficial for retaining shallow features of input images. Therefore, U-Net is used in this study for CNN-based segmentation of foam grayscale images. The basic structure of U-Net is shown in Figure 3. Overall, the U-Net network contains 7.7 M trainable parameters with a calculation size (indicating the forward/backward pass size) of 109 MB.

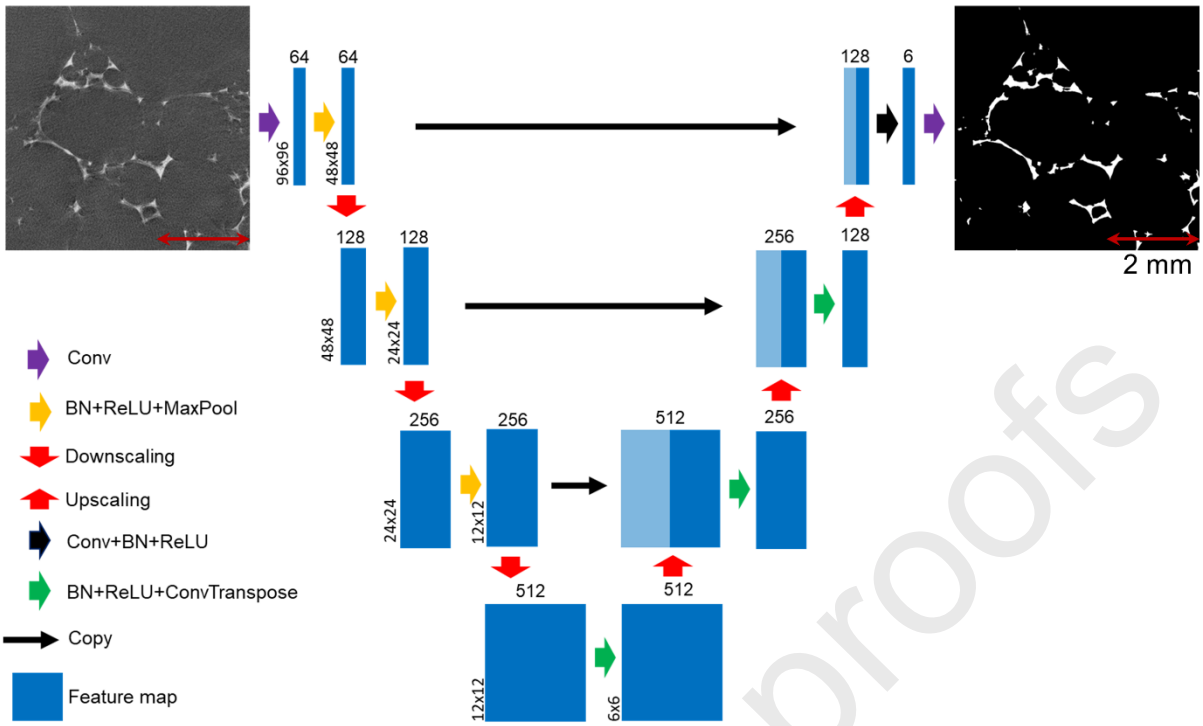

Figure 3: Architecture of symmetric encoding-decoding U-Net, containing long skip connection linked between encoding layers to decoding layers. The input image contains three channels, and the output has two channels, indicating foam phase and background.

2.3.5 U-ResNet segmentation

U-ResNet is an extended network of U-Net with residual skip connections. The short skip connection is one of the primary reasons why ResNet outperforms other network structures in image classification (He et al., 2016). Therefore, U-ResNet takes the advantages of both the long skip connection used in U-Net and the short skip connection used in ResNet, as shown in Figure 4. U-ResNet contains an encoding step and a decoding step, including 4 encoding blocks that extract different levels of features from the input image and 4 decoding blocks that transpose these features into the segmented output image. Shallow features are then retained by the skip connections. Overall, the network contains 8.2 M trainable parameters, and the calculation size (indicating the forward/backward pass size) is 138 MB.

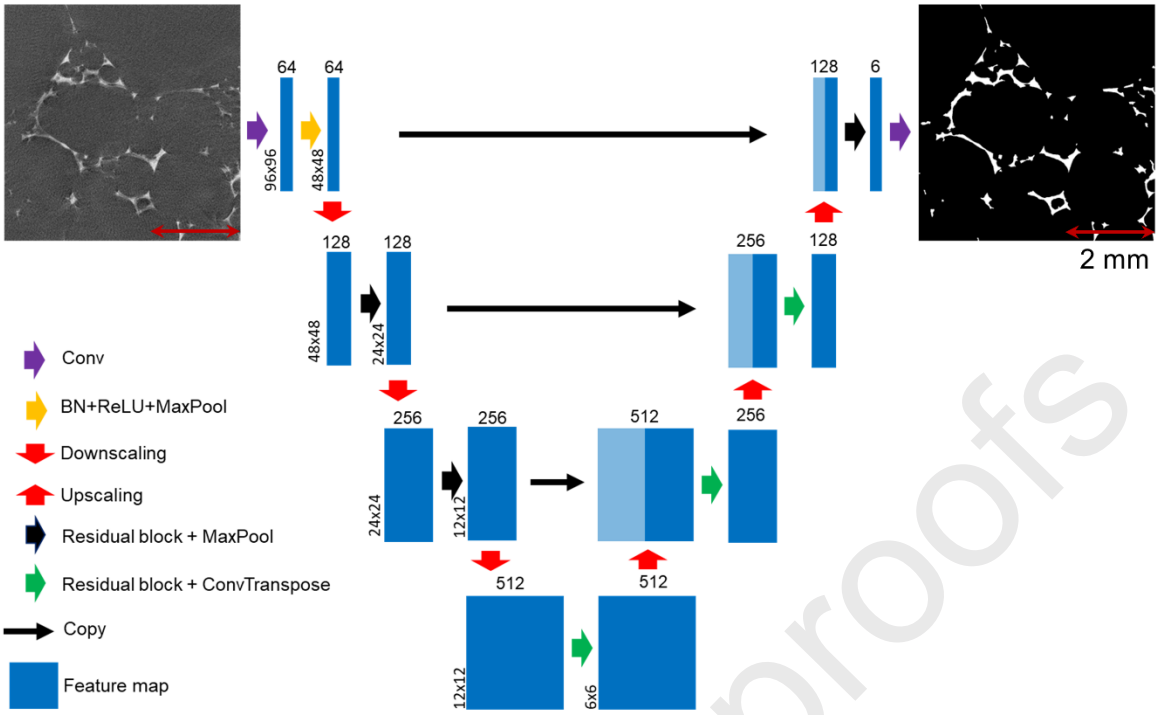

Figure 4: Architecture of U-ResNet, containing both short skip connection (Residual block) and long skip connection. The input image contains three channels, and the output has two channels, indicating foam phase and background.

2.3.6 EfficientU-net segmentation

Apart from the encoder-decoder symmetric network, EfficientU-Net is an encoder-decoder asymmetric structure that uses a network pre-trained on ImageNet for image classification and feature extraction. In this study, a state-of-art pre-trained EfficientU-Net (Tan and Le, 2019) with its advantage of high training efficiency by balancing network depth, width, and resolution, is used as the feature extractor. During the decoding step, a concept like U-Net and its long skip connection is used to transpose features back to the segmented output image. Therefore, the overall encoder-decoder asymmetric network is used to test its segmentation performance. The network architecture is shown in Figure 5. The total trainable parameters are 32 M. However, due to its high efficiency, the calculation size (indicating the forward/backward pass size) is 86 MB, which is only 62% of U-ResNet.

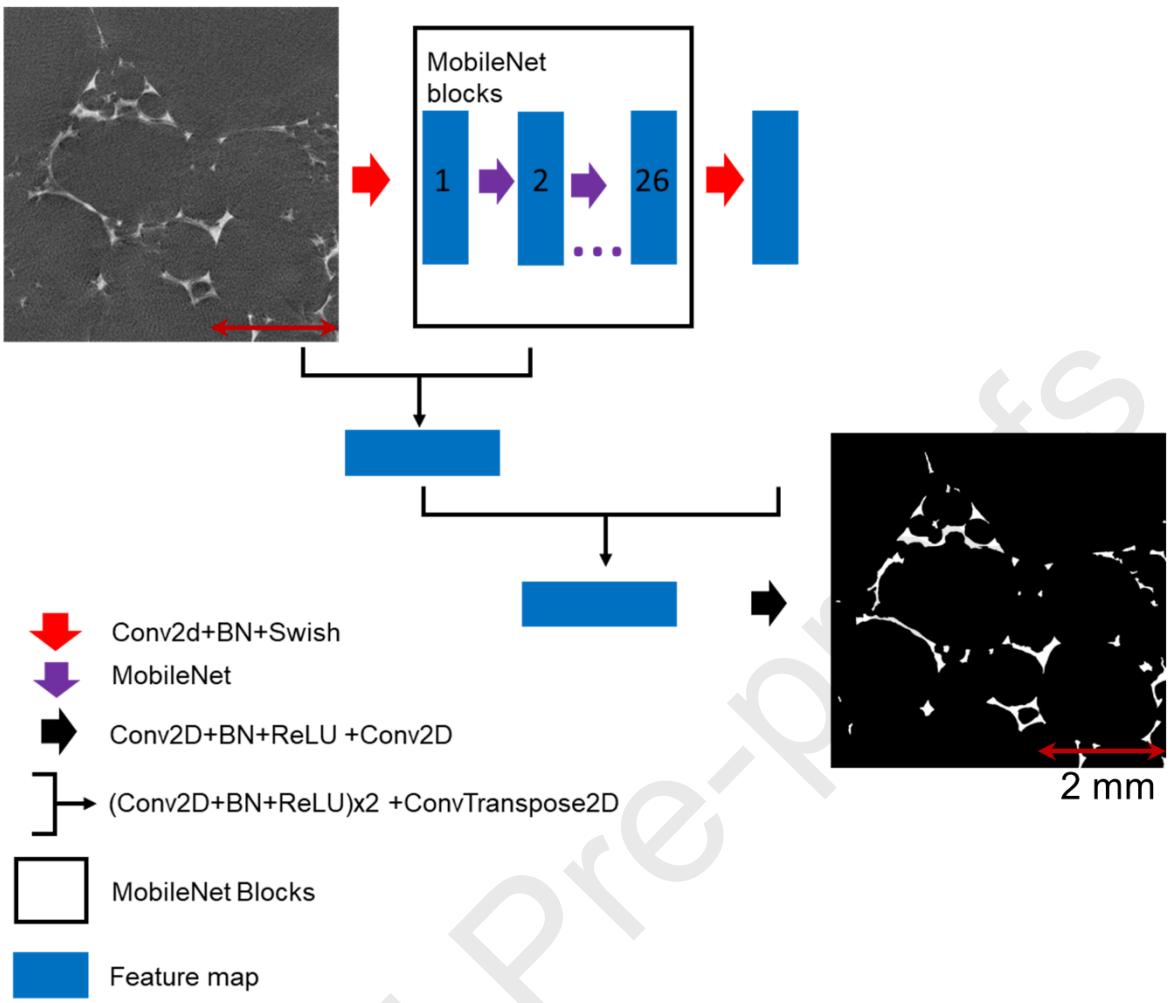

Figure 5: Architecture of EfficientU-Net-B3. The encoder contains several MobileNet blocks. The decoder contains several upsampling layers with long skip connections between encoding layers.

2.4 Foam quantification

The bubble volume and liquid fraction of the 3D binary segmented images for the two MFC concentrations and various aging times were measured in Avizo™. The liquid fraction (ϕ) was measured on the raw segmented images. However, to measure bubble size, the conjoint air bubbles due to resolution limitations, i.e. partial volume effect (Clausnitzer and Hopmans, 1999), were separated using the "separate objects" tool, and the "opening" filter was applied to remove any objects with less than 3 pixels to minimize error in bubble size measurements due to noise. Finally, the "label analysis" function was used to measure the bubble volume (V). Since most of the bubbles were highly spherical, the bubbles were assumed to be fully spherical, the volume-equivalent diameter (d_i) was calculated as

$$d_i = \sqrt[3]{\frac{6V}{\pi}}. \quad (2)$$

The volume-equivalent diameters (d_i) were then used to calculate the Sauter mean diameter (d_{32}). The d_{32} for the total number of bubbles N present in the foam structure is calculated as

$$d_{32} = \frac{\sum_{i=1}^{N} d_i^3}{\sum_{i=1}^{N} d_i^2}. \quad (3)$$

Also, the Plateau border diameter (D_{PB}) and node radii (D_{node}) of the 0.025% and 0.05% MFC foams were estimated from the micro-CT images using pore network extraction (Muin et al., 2020). Implementation of pore network modelling (PNM) on the segmented liquid phase of the foam image provides spherical pores that correspond to foam nodes, and cylindrical connections that correspond to Plateau borders (PB) distributed across the foam structure, as shown in Figure 6.

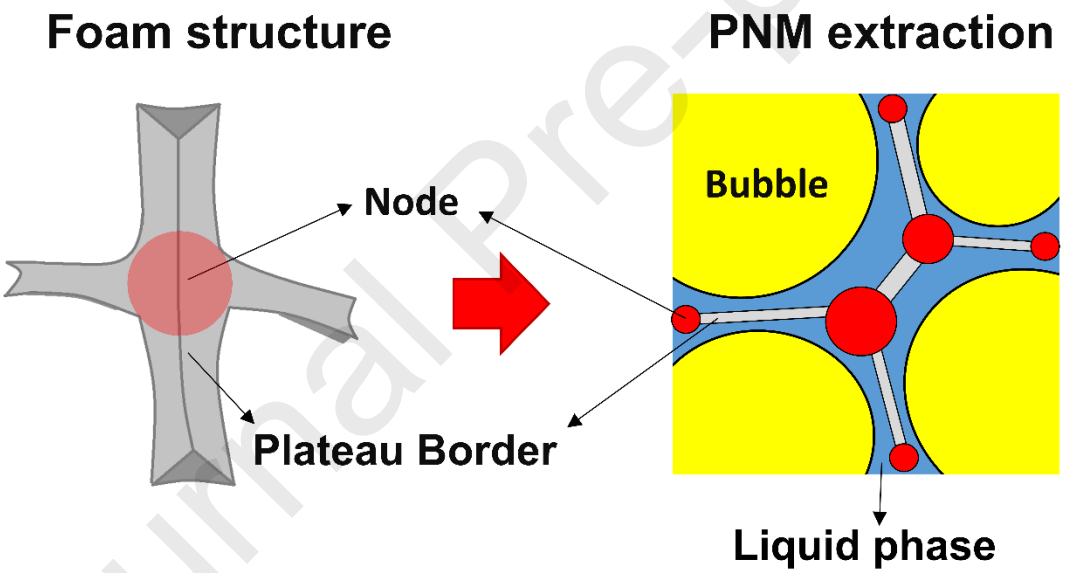

Figure 6: Application of pore network modelling (PNM) to estimate the size of Plateau borders and nodes

Lastly, confocal images and liquid rheology measurements of the MFC foam samples at 0.025% and 0.05% were obtained to help explain the bulk and microscale observations made. The confocal scans were acquired using the Zeiss LSM 880 inverted confocal laser scanning microscope (CLSM) that utilizes an Airyscan module, while the liquid rheology measurements were obtained using the Discovery HR-1 hybrid rheometer for the two MFC concentrations.

3. Results

The fast-aging dynamics of the MFC foams are evaluated by implementing EfficientU-net segmentation. Firstly, quantitative findings that justify the usage of EfficientU-net are covered followed by a 3D microscopic study of the foam dynamics. The unique stabilization mechanism of MFC foams is elucidated along with the identification of the dynamic aging mechanisms that occur prior to the foam being arrested by the MFC.

3.1 Bulk stability of MFC foams

High-resolution time-lapse images were used to identify how the bulk foam evolves with respect to foam aging time. It is evident from that as the MFC foams drain, the foam-liquid interface moved upwards as liquid accumulated at the bottom of the foam phase. However, the position of the foam-liquid interface in

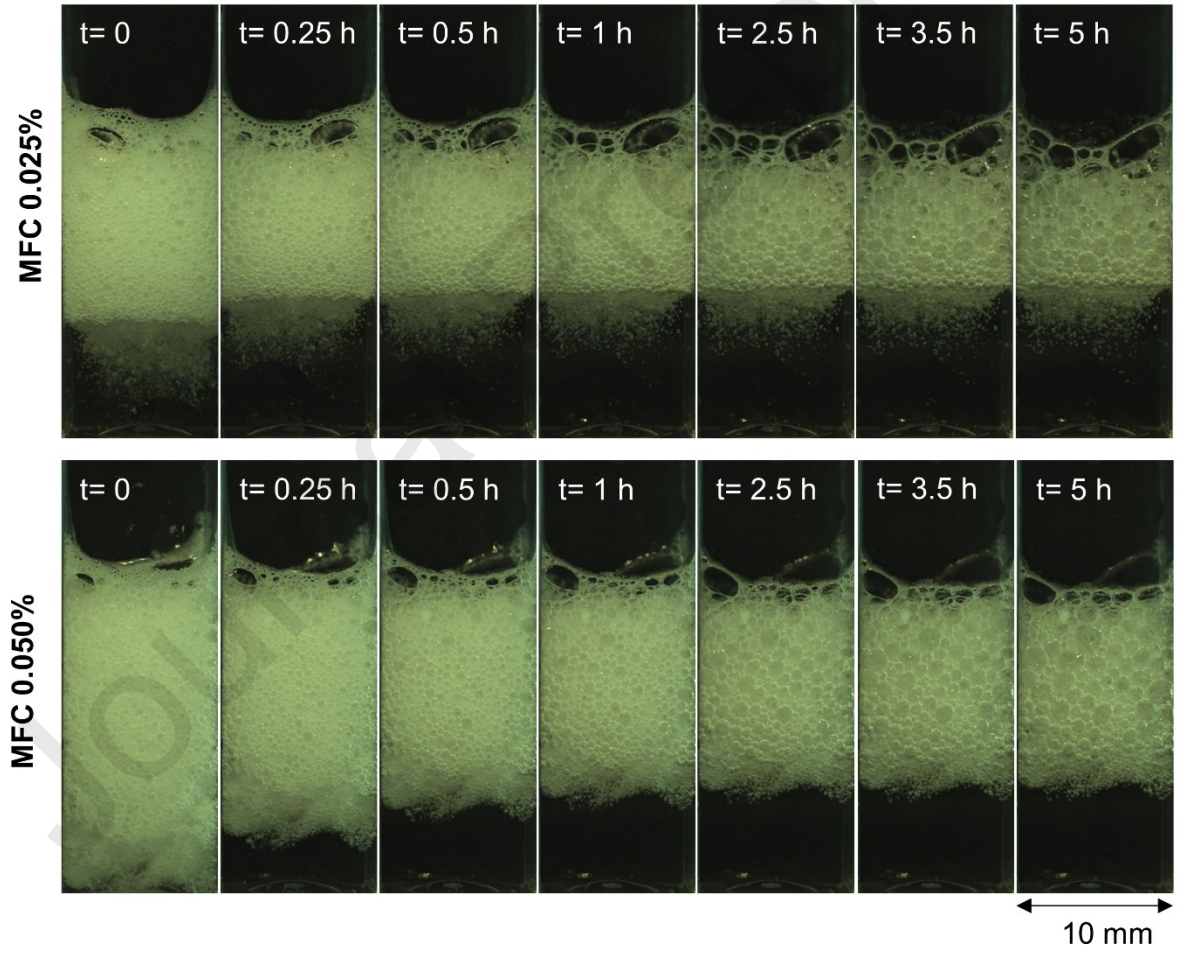

Figure 7 remained static after approximately *t*= 0.25 h and *t*= 0.5 h for the 0.025% and 0.05% MFC, respectively. At this point, a balance between drainage and capillary forces was achieved and an equilibrium liquid distribution profile was established (Magrabi et al., 2001; Neethling et al., 2005).

This compared well with the theoretical free drainage times (Rio et al., 2014) of 0.27 hours and 0.58 hours (see Appendix 7.1) for the 0.025% and 0.05% MFC foams, respectively.

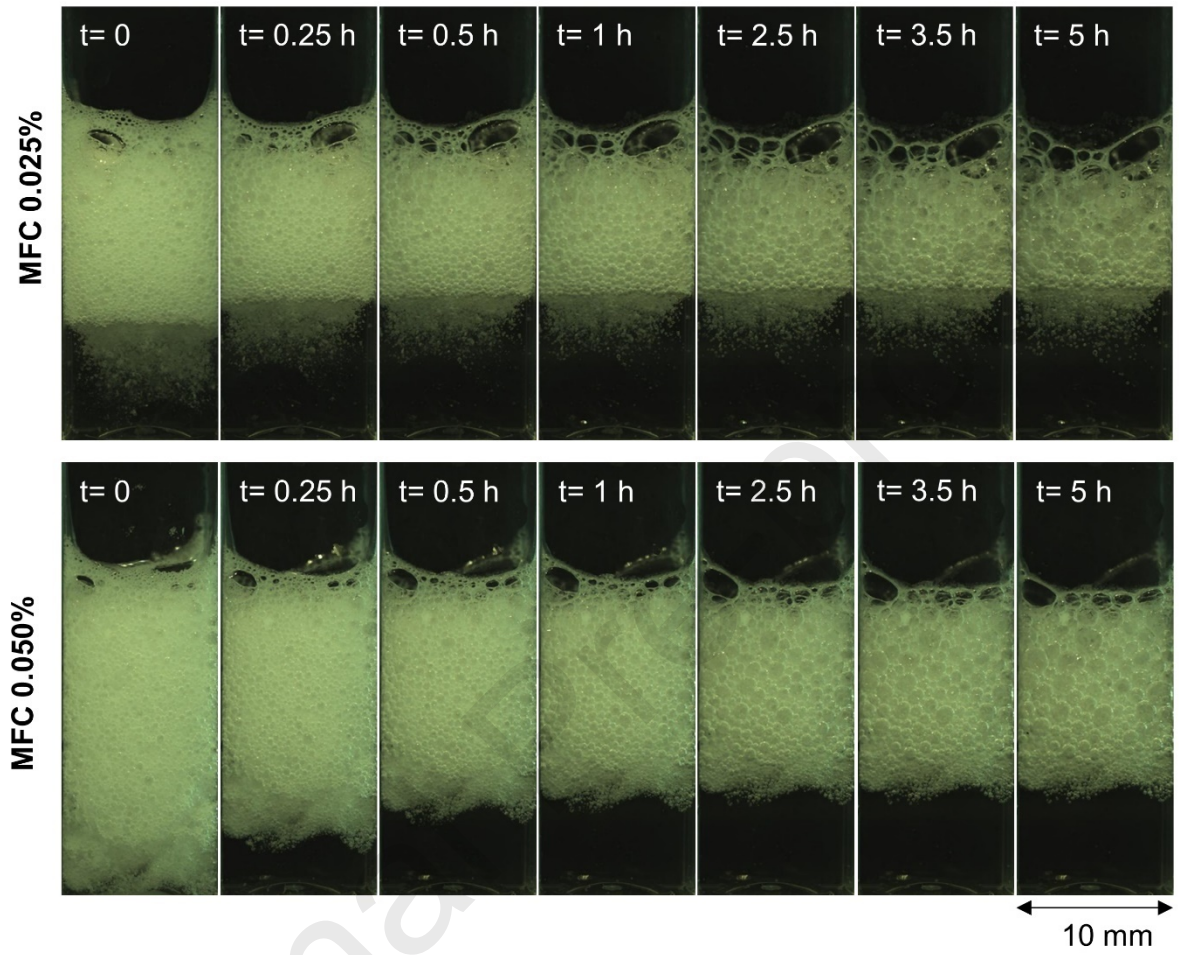

Figure 7: Time-lapse images of the bulk foam between t= 0 to 5 hours with MFC concentrations of 0.025% and 0.05%. The position of the foam-liquid interface remains relatively static after free drainage has completed at approximately *t*= 0.25 hours and 0.5 hours for the 0.025% and 0.05% MFC foams, respectively.

Average foam volume ($V_{f,\,avg}$) versus *t*, based on 3 replicates, is provided in Figure 8 based on quantitative analysis of the images in Figure 7. For both 0.025% and 0.05% MFC foams, a rapid decrease in $V_{f,\,avg}$ over *t* was observed within the initial 0.5 hours of aging in Figure 8. This observation corresponds well with the theoretical free drainage times reported in Appendix 7.1 and

the bulk foam stability observed in

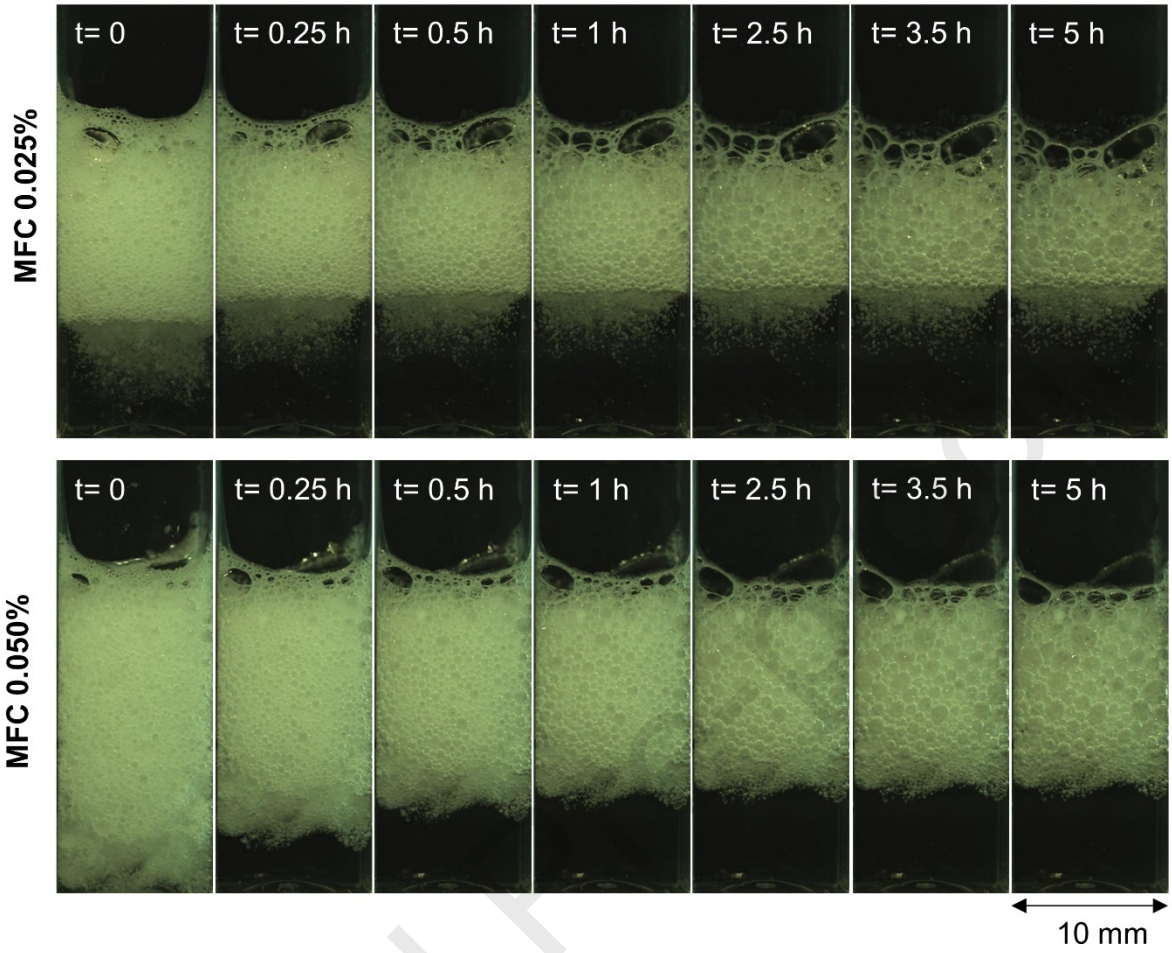

Figure 7. After the free drainage regime is completed, a steady decrease in $V_{f,\,avg}$ versus t was observed that appears to be non-linear. In this intermediate regime, the rate at which $V_{f,\,avg}$ decreases also declines. Finally, the foams are considered arrested when the $V_{f,\,avg}$ remains relatively constant. This point is defined as the earliest time at which $V_{f,\,avg}$ decreases no more than 0.1% over 30 minutes (see Figure 8). Thus, the time taken for the 0.025% and 0.05% MFC foams to fully arrest was calculated as 84.3 hours and 26.5 hours, respectively. Hence, in the intermediate region, i.e., after the free drainage regime and before the foam arrest, we expect that micro-scale drainage occurs due to the onset of diffusive coarsening and coalescence events, consistent with the evident increase in bubble size in Figure 7 with time. Coarsening and coalescence of the foam will be discussed in further detail in Section 3.4.

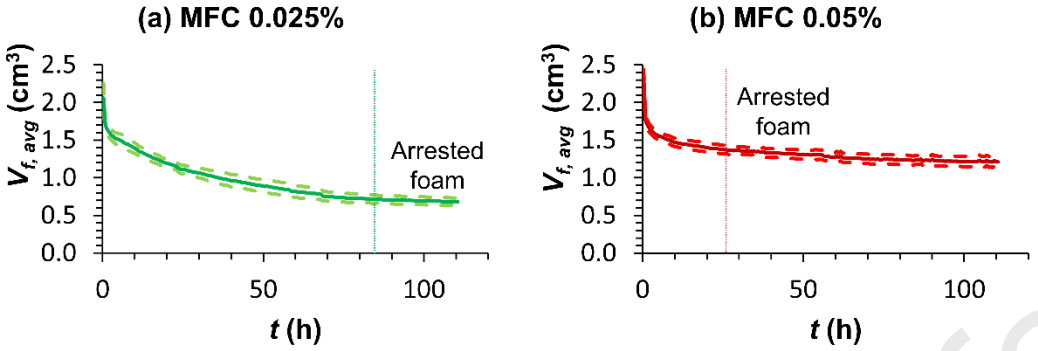

Figure 8: Plot of average foam volume $V_{f,\,avg}$ in cm^3 versus foam aging time t in hours illustrates that the foam volume remains stable on the order of few days due to the arresting behavior of the liquid phase. The bulk foams arrest at approximately 84.3 hours and 26.5 hours as indicated by the vertical lines for the (a) 0.025% MFC and (b) 0.05% MFC, respectively. The dashed curves provide the standard error in the $V_{f,\,avg}$ measurements that are based on three replicates.

Hence, the data presented in Figure 7 and Figure 8 suggest that micro-CT imaging will be challenging during the initial aging time, i.e. t< 0.5 hours when rapid dynamics in foam structure are expected. Moreover, it suggests that shorter scan time in the order of minutes is required to minimize possible motion artifacts and capture the fast-aging dynamics at early times. Thus, to test the limitations of imaging foam dynamics with micro-CT and evaluate the capabilities of advanced machine learning approaches to extract quantitative data, we focused on aging times immediately following the free drainage regime to evaluate the various approaches for image segmentation. We will then investigate the structural dynamics over time to understand the fundamental mechanisms that drive the processes observed in Figure 8.

3.2 Impact of scan time on micro-CT images

For static objects, longer scan times provide higher SNR, which is the main rationale for a scan of many hours (Bultreys et al., 2016). To assess the impact of scan time on image quality for dynamic samples, two micro-CT images of the 0.025% MFC foam at t = 9 hours, prior to foam arrest (see Figure 8) were acquired. The micro-CT images with scan times of 5 and 30 minutes are shown in Figure 9a. Reduced motion artifacts were observed with the shorter 5-minute scan compared to the longer 30-minute scan, which had significant streaking artifacts caused by movement (Park et al., 2015). However, the 5-min scan appeared granulated within the homogenous regions with an observable broad range of grey-scale values.

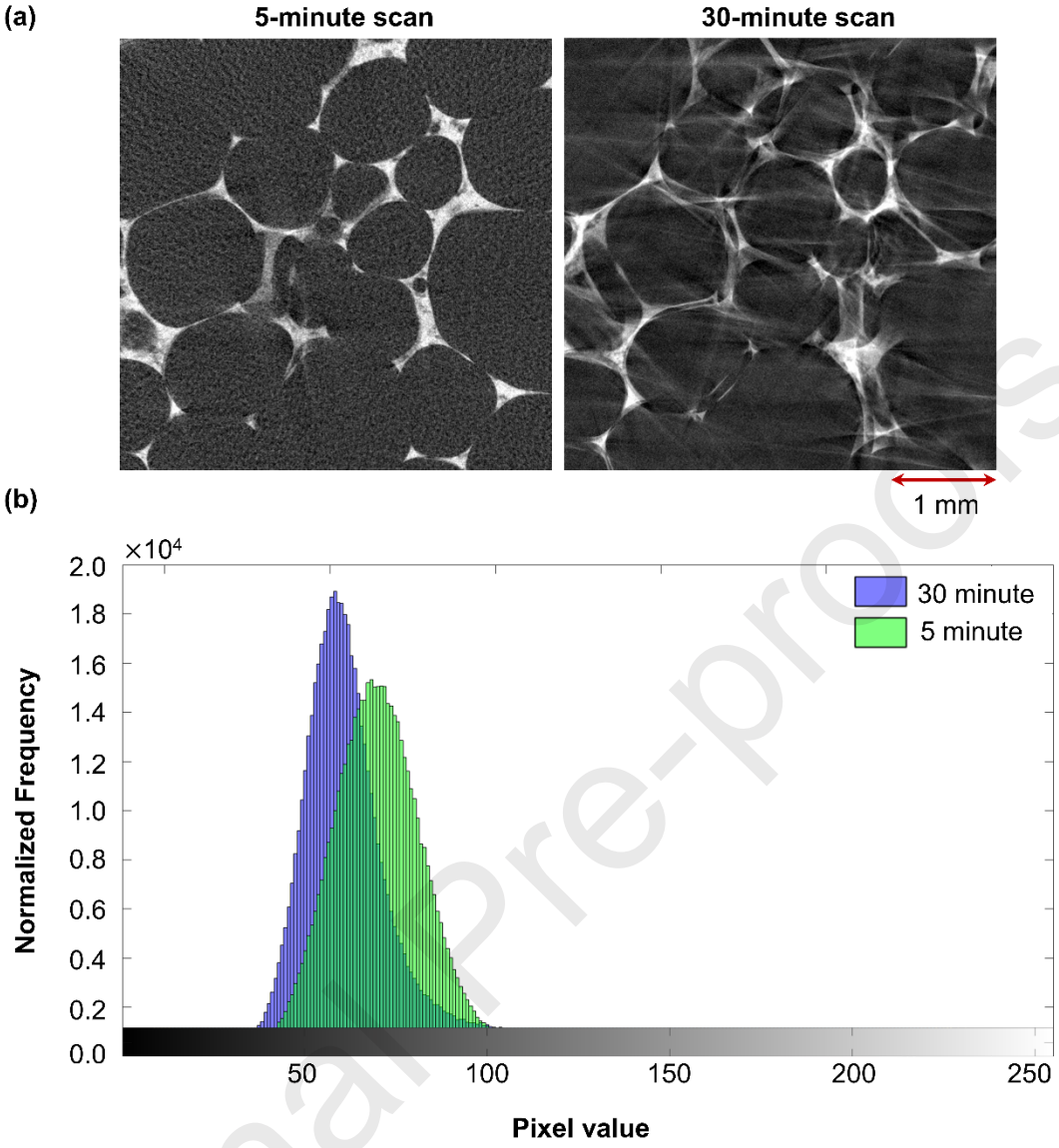

Figure 9: (a) Example of a 5-minute scan (left) followed by a 30-minute scan (right) of the same foam sample where the darker greyscale values represent the less dense air phase and lighter greyscale values represent the denser liquid phase; (b) Frequency distribution of the greyscale pixel values ranging from 0 to 255. The 5-minute scan shows a broader peak compared to the narrower peak for the 30-minute scan due to the presence of higher noise levels in the shorter 5-minute scan.

The frequency distributions of the greyscale voxels for the 5-minute and 30-minute scans are provided in Figure 9b. Broader distribution is observed for both the scans without well-defined peaks for the liquid and air phases. As observed in Figure 9a, the motion artifacts, represented by the higher pixel values, in the 30-minute scan are significant, resulting in poorly resolved gas cell interfaces. This also aligns with the plot of $V_{f,\,avg}$ versus t for the 0.025% MFC foam shown in Figure 8a, where the foam aging mechanisms are dynamic at t= 9 hours since the bulk foams arrest at a much later time of about 84.3 hours.

Relatively fast dynamics also result in motion artifacts for the 5-minute scans during the early stages of foam aging. This is observed in Figure 10 where several 5-minute scans are presented for the first 1 hour of aging. For both MFC concentrations, the image quality significantly improves for aging times greater than 30 minutes, as the foam dynamics slow down. The air-liquid interfaces do not become sharp until after approximately 30 minutes. Evidence of coalescence (shown with red arrows) and diffusive coarsening (shown with yellow arrows) in the first hour of foam aging is evident in Figure 9. For the coalescence zones, two bubbles merge and become a larger bubble while in the diffusive coarsening zone, the smaller neighboring bubble shrinks while the larger neighboring bubble grows.

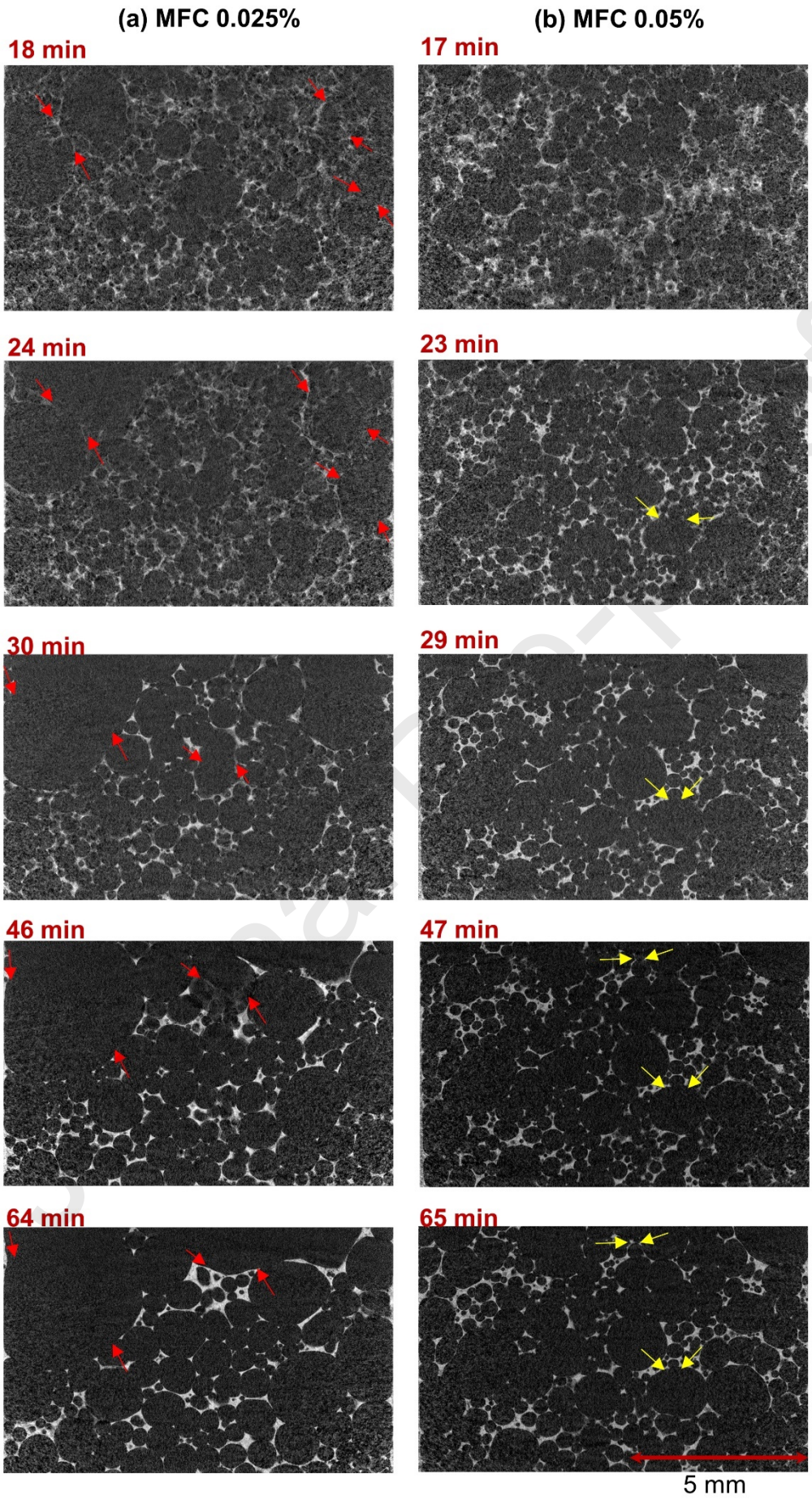

Figure 10: Demonstration of image quality for the MFC foams at 0.025% and 0.05% bulk fiber concentrations at various aging times. Enhancement in image quality is observed for t>30 minutes as the foam dynamics slow down. The presence of coalescence events is indicated by red arrows and diffusive coarsening regions are indicated by yellow arrows. For the coalescence events, two bubbles merge while in a diffusive coarsening region, a smaller neighboring bubble shrinks while the larger neighboring bubble grows.

3.3 Justification: image segmentation technique

The approach for segmenting the dynamic foam images was carefully selected by comparing its performance over 3 million pixels of GT data. Afterwards, the accuracy of each segmentation method was quantified and the technique yielding the least absolute error was chosen to segment the MFC foam images.

To quantify the quality of segmentation, an average error rate (ε_{avg}) was calculated by averaging the percentage errors in the measurement of Euler characteristic (χ), liquid phase area (A_l), and air phase area (A_g). The results are shown in Table 2. Overall, EfficientU-net provided the least average error (ε_{avg}) of 11.5%, which is a significant error reduction from the traditional segmentation method involving the NLM filter followed by watershed segmentation, which resulted in a significantly higher ε_{avg} of 28.0%. In addition, EfficientU-net was significantly more effective at minimizing the error in χ measurements. The χ provides an indication of the connectivity of the liquid phase and is a crucial metric that determines the accuracy of numerous quantitative measurements, such as permeability, and other transport processes in complex media (Armstrong et al., 2019). Hence, greater accuracy of χ means that simulations or modeling work on the segmented images would be more reliable.

Table 2: Percentage errors in the measurement of Euler characteristic (χ) of the liquid phase, Total area of liquid films (A_l), and Total area of air bubbles (A_g) with respect to the GT to compare the performance of the different CNN techniques. The reported figures are generated using the average of three 1000x1000 pixels GT slices. The average error (ε_{avg}) presented in the last row is an average of the errors for χ, A_l, and A_g. EfficientU-net demonstrates the least average error across all the segmentation techniques as shown in the last row.

% error	**U-Net**	**U-Resnet**	**EfficientU-net**	**Watershed**
χ of liquid phase	59.8	38.9	32.4	82.4
Total area of liquid films (A_l)	1.39	0.476	0.136	0.109
Total area of air bubbles (A_g)	19.6	6.71	1.87	1.54
Average error rate (ε_{avg})	26.9	15.4	11.5	28.0

Overall, it is deduced from Table 2 that EfficientU-net provided the closest match to the GT data in comparison to the other segmentation techniques. Nonetheless, the percentage errors in total bubble area and total liquid film area for the EfficientU-net and watershed segmentation are quite similar, which suggests that further investigation is required to delineate between these two segmentation methods.

To further evaluate the performance of the CNNs and traditional segmentation, the frequency of wrongly assigned pixels with respect to the GT data was plotted as a function of distance from an interface. The results based on 3 x 10^6 pixels of GT data are presented in

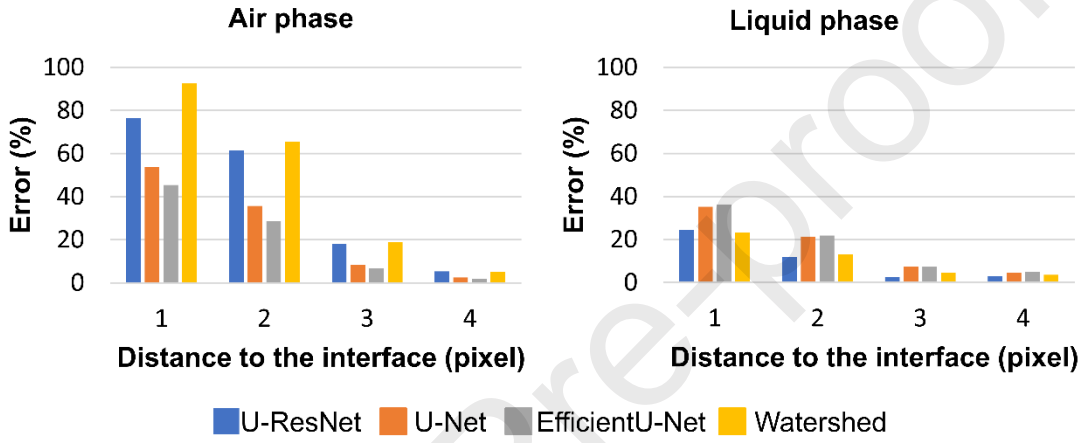

Figure 11. It is evident that the air-liquid interface experiences the highest frequency of misidentified voxels. The percentage error is relatively high for locations at a one-pixel distance from the interfaces in

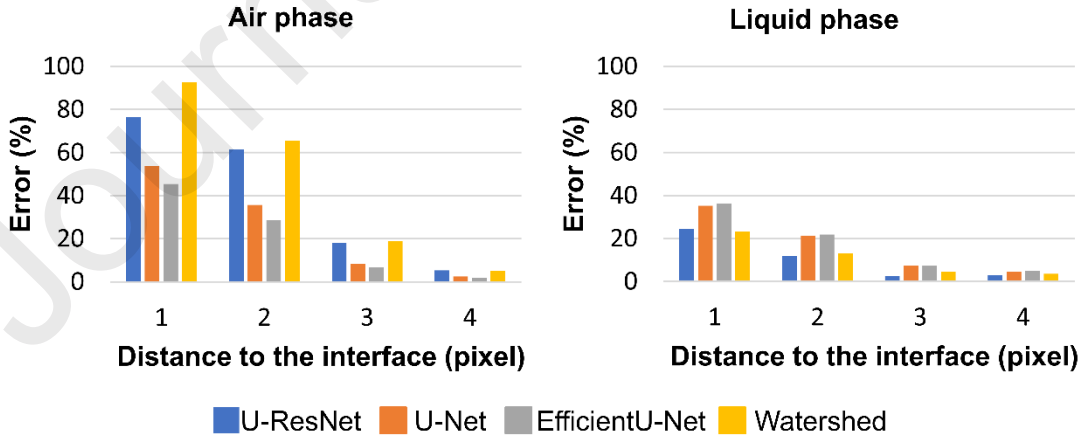

Figure 11, even though the percentage errors for bulk geometrical measurements in Table 2 are relatively low. This trend is expected since the interfacial regions are highly difficult to segment.

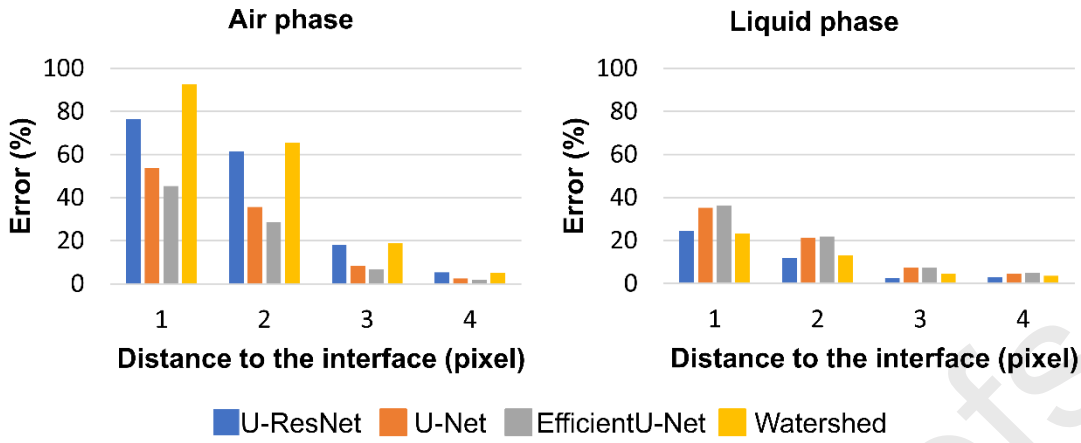

Figure 11: Histogram of percentage of error pixels with respect to distance from the interface. The error level is higher closer to the interface due to the low SNR of the micro-CT images. It is observed that the U-ResNet and Watershed underestimate the liquid phase while the U-Net and EfficientU-Net underestimate the air phase. The total number of pixels within a distance of pixel=4 from the interface is 43075.

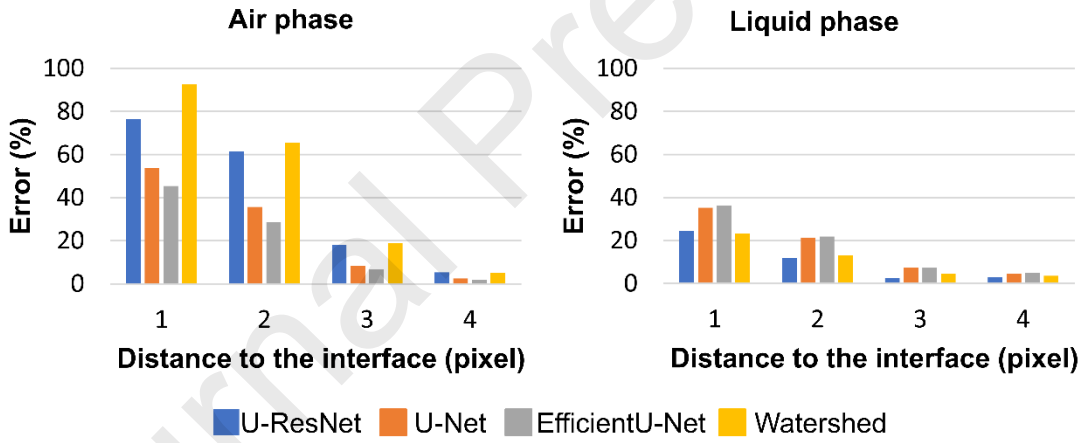

Figure 11a demonstrates that watershed segmentation had the highest frequency of misidentified voxels within the air phase that are one-pixel distance from an interface; on the other hand,

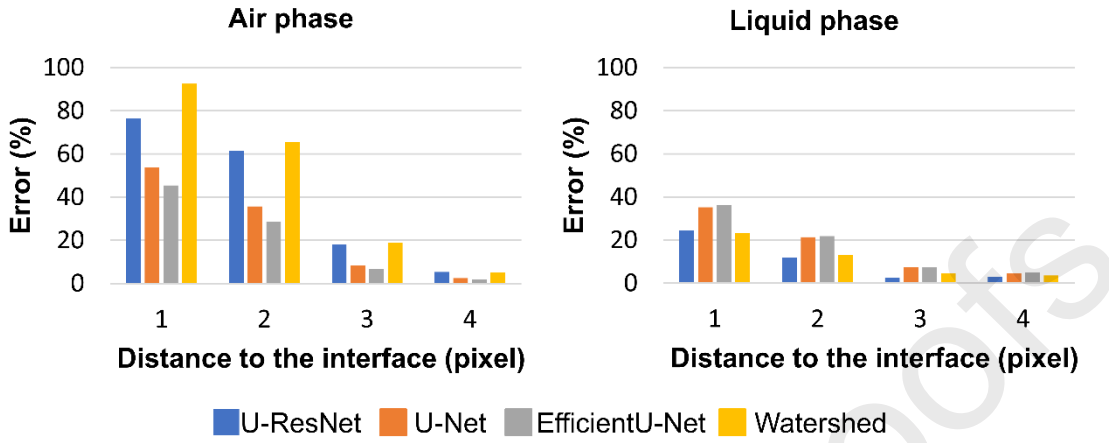

Figure 11b demonstrates that EfficientU-Net had the highest frequency of misidentified pixels within the liquid phase that are a one-pixel distance from an interface. To gain an overall understanding of which segmentation technique provided the most accurate segmentation of the interface, the sum of the misidentified pixels at a one-pixel distance was calculated. As presented in Table 3, Efficient U-net had the lowest sum of misidentified pixels at a one-pixel distance from an interface. One possible explanation is that EfficientU-net yields higher accuracy due to the pre-trained B3 structure, which is absent in U-Net and U-ResNet, and thus may provide a better feature extraction encoding process (Tan and Le, 2019).

Table 3: Frequency of misidentified pixels for the air and liquid phases at a distance of one pixel from the air-liquid interface. The highest accuracy is achieved with EfficientU-net, which consists of the least overall sum of misidentified pixels. The total pixels present in the image at a one-pixel distance are 10750.

Error pixel frequency	**U-Net**	**U-ResNet**	**EfficientU-net**	**Watershed**
Air phase	2930	4169	2475	5039
Liquid phase	1869	1292	1930	1227
Overall Sum	4799	5461	4405	6266

Given the overall performance, it was decided that EfficientU-net was the most suitable segmentation method to study the MFC foam. This was based on bulk geometrical measures and pixel identification near the air/water interface. Both performance measures are particularly

important when studying the physics of a system controlled by interfacial forces, and thus the geometry of interfaces is of utmost importance.

3.4 Evaluation of the MFC foam dynamics

As previously observed in Figure 10, there was significant movement due to foam drainage for t< 30 minutes. The first image that could be segmented was collected approximately 45 minutes after foam generation. The initial bubble size distributions for the two MFC concentrations at 45 minutes are presented in Figure 12. Higher polydispersity of the foam bubbles was observed for the lower MFC concentration at early aging times in Figure 12, which provides the surface renderings and initial bubble size distributions for the MFC foams. To confirm this, polydispersity was estimated using the polydispersity parameter (p_{32}) which is calculated using the Sauter mean diameter (Drenckhan and Hutzler, 2015; Kraynik et al., 2004) for the two MFC foams. The p_{32} for the 0.025% MFC foam was 0.172, and 0.05% MFC foam was 0.037 at t= 45 minutes, which means that the 0.025% MFC foam system was more polydisperse.

The difference in polydispersity observed at approximately t= 45 minutes was primarily attributed to the dynamics during foam generation. The bulk viscosity of the MFC fluid was expected to be higher at 0.05% MFC, which means that the bubbles are less likely to coalesce during foam production, which would produce a more uniform size distribution of bubbles. With the 0.025% MFC concentration, however, the degree of coalescence is presumably higher as the bubble lamellae can rupture more easily in a less viscous medium, and thus form a wider range of initial bubble sizes. The bulk rheological measurements of the MFC fluid at 0.025% and 0.05% are provided in Figure 13b where the viscosity is three times higher for the 0.05% MFC concentration at low shear rates. The lowest shear rate used in the measurement was approximately 1 s^{-1} which was considered to be representative of a slowly draining foam (Safouane et al., 2006). Overall, the difference in viscosity influenced the foam formation process, which impacted the initial size distribution.

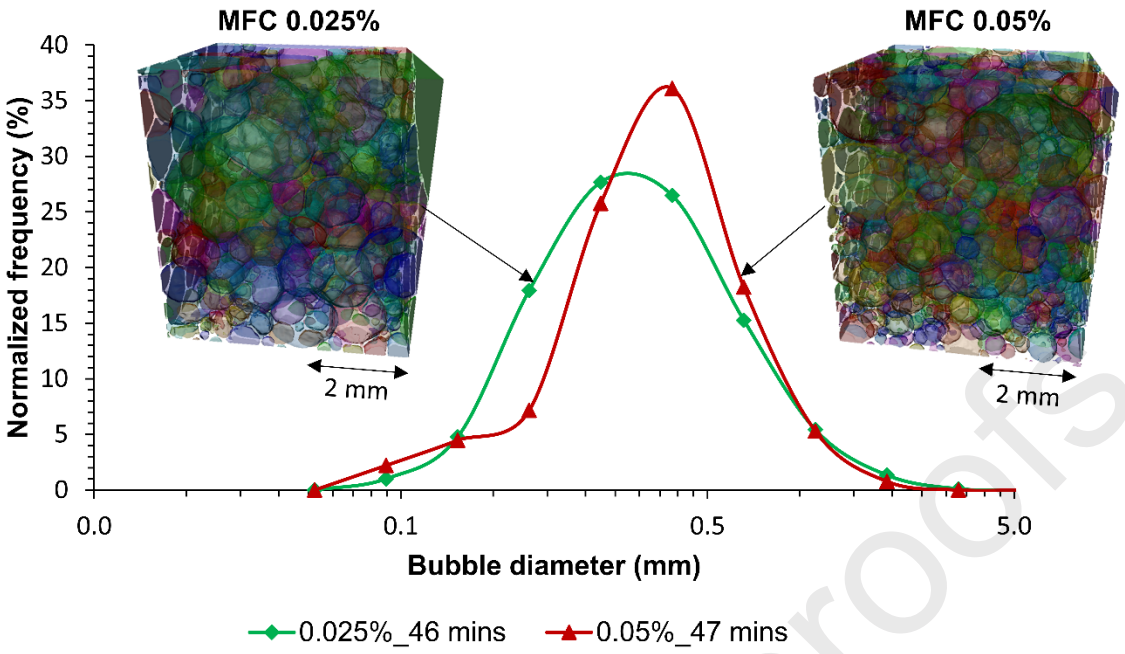

Figure 12: Higher polydispersity is observed for the 0.025% MFC foam. This is attributed to the higher degree of coalescence experienced at the 0.25% MFC concentration during foam generation.

The rheology of the interstitial fluid present in the MFC foam was strongly influenced by the extent of fiber entanglement. Figure 13 presents the CLSM images showing the MFC structure within the foam lamellae and provides the rheological measurements at the two MFC concentrations. While the cellulose fibers were nanometer in diameter, they were micrometer in length and formed an entangled scaffolding-like network (Pääkkö et al., 2007) that spans across the Plateau borders and nodes of the foam structure, see Figure 13a. It is known that the entanglement of the cellulose fibers results in yield stress that inhibits the liquid phase to flow (Iotti et al., 2011; Tatsumi et al., 2002). Hence, the viscosity is higher with the 0.05% MFC concentration as it can presumably form a more entangled network due to the higher density of fibers present in the dispersion (Martoïa et al., 2016; Song et al., 2019a, b). As observed in Figure 13b, the difference in viscosity versus MFC concentration was most significant at lower shear rates as would be expected during foam aging. At high constant shear rates, the entangled fibers align along flow lines and disentangle, causing a reduction in viscosity (Iotti et al., 2011; Karppinen et al., 2012; Saarikoski et al., 2012). Typically, the likelihood of entanglement increases with fiber length and decreases with fiber diameter (Hill, 2008; Mendoza et al., 2018; Pääkkö et al., 2007). Overall, the entanglement of the MFC fibers is responsible for the shear-thinning behavior and the effective viscosity of the dispersion medium.

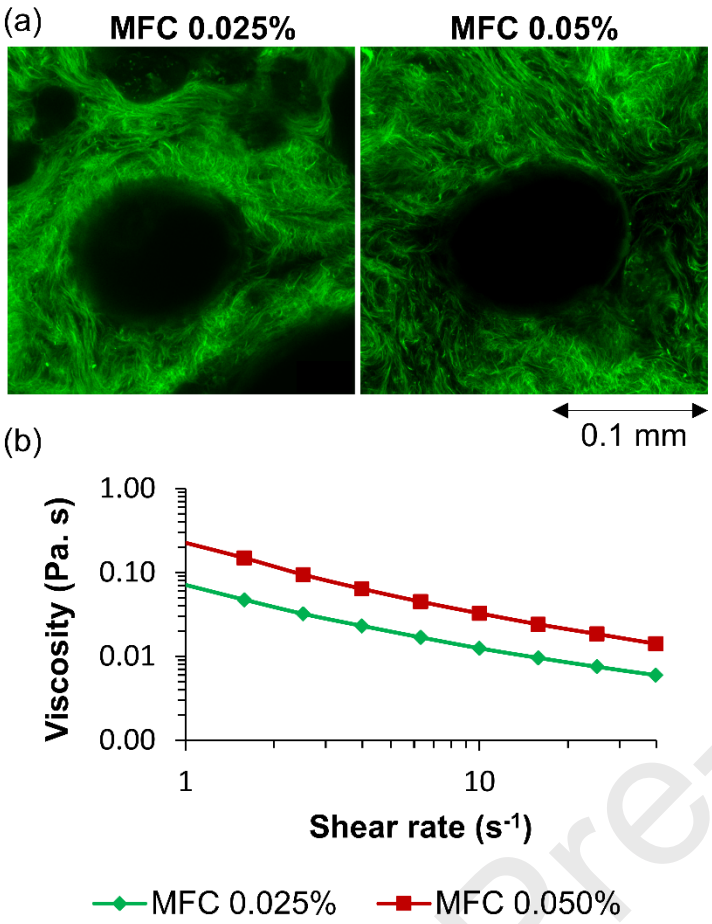

Figure 13: (a) Confocal images of the foam phase for 0.025% and 0.05% MFC, and (b) Bulk liquid viscosity versus shear rate for 0.025% and 0.05% MFC. The entanglement of the high aspect ratio MFC nanofibers results in yield stress that inhibits the liquid phase to flow. The foam bubbles surrounded by the 0.05% of MFC fibers experience higher viscosity and higher yield stress than 0.025% as the shear rate from the foam preparation method is relatively low.

Variation in the foam drainage rates was observed between the two MFC concentrations. Figure 14 shows that the liquid fraction of the 0.025% MFC foam was nearly constant between 45 to 65 minutes, but the liquid fraction values for the 0.05% MFC decreased in this time interval. This is attributed to the yield stress of the interstitial fluid, which increases as a function of MFC fiber concentration (Song et al., 2019a). Hence, for the 0.05% MFC foam the interstitial fluid must overcome greater yield stress to drain through the network of Plateau borders and nodes. This means that free drainage occurs over a greater timescale, and while free drainage has completed for the 0.025% MFC in the first 30 minutes, the 0.05% MFC foam continues to drain for the first hour. This behavior aligns with the estimated free drainage times provided in Appendix 7.1 and is also

captured in

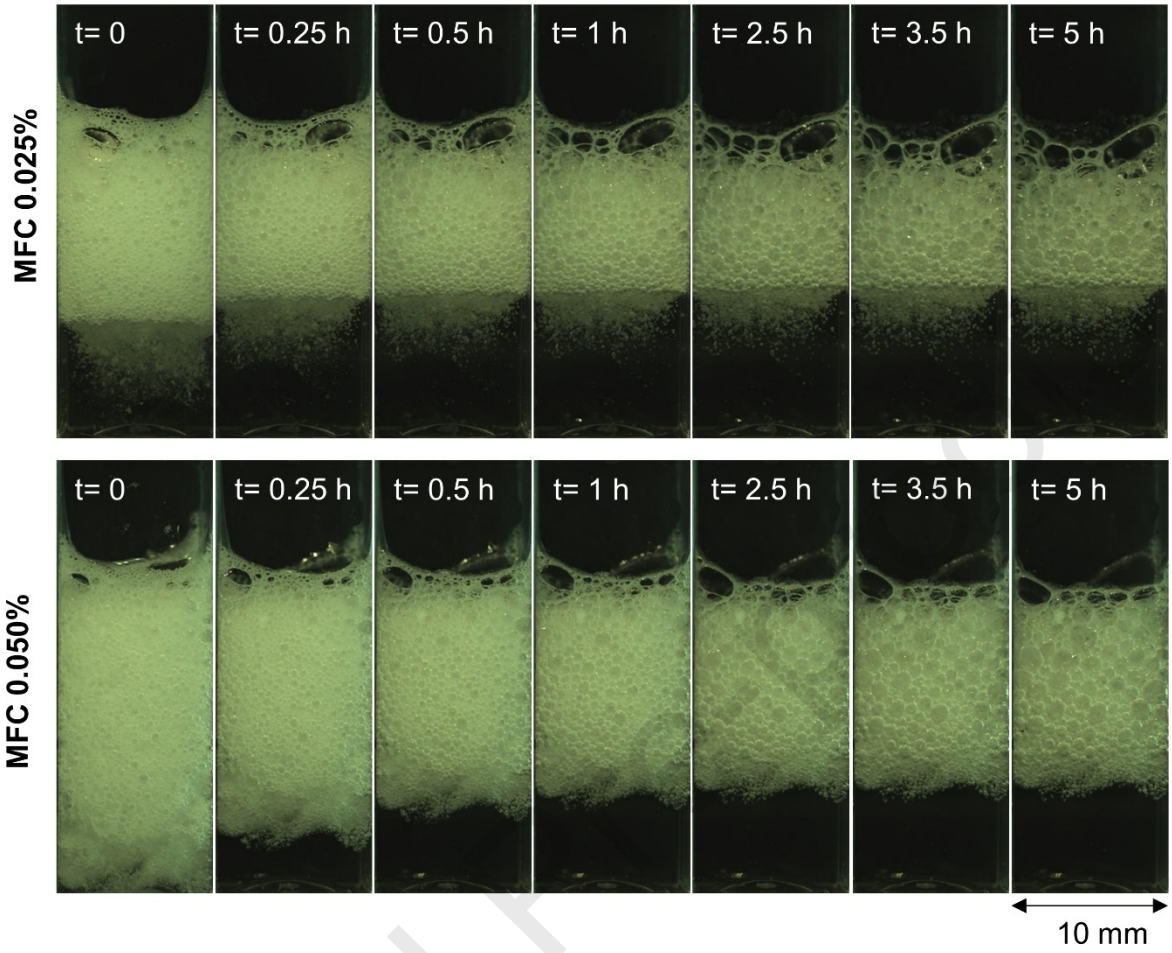

Figure 7 where the foam-liquid interface for the 0.05% MFC foam continues to rise within the first hour of aging, but the foam-liquid interface remains relatively static for the 0.025% MFC foam.

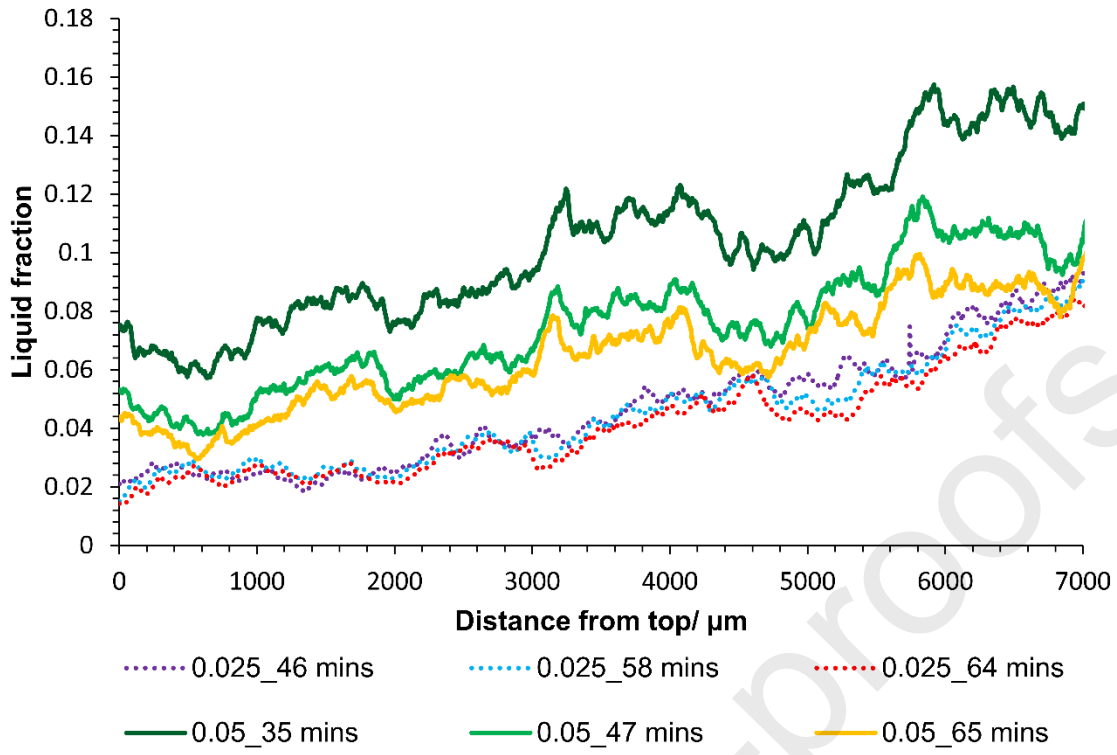

Figure 14: Plot of liquid fraction versus distance from the top of the foam image for MFC concentrations of 0.025% and 0.05%. The liquid fraction for the 0.05% MFC remains almost constant while the liquid fraction of the 0.025% MFC decreases over time. This behavior represents the higher yield stress of the 0.05% MFC fibers which decelerate foam drainage and elongate the timescale for the free drainage regime.

As previously seen in Figure 8, the liquid phase appears to become arrested at late time. It is hypothesized that the MFC concentration within the liquid phase increases as the foam drains. Once a critical MFC concentration is obtained the foam is arrested, and thus foam volume versus time becomes relatively static. This would occur if the MFC remains within the PB channels as the liquid drains, resulting in an increased concentration. To check if physical clogging of the MFC fibers could occur, the PB and node diameters within the liquid phase were measured using pore network modeling (Muin et al., 2020). The nodes are the locations where multiple PBs come together. The network distributions are provided in Figure 14. At 45 minutes, the average PB diameter was approximately 90 micrometers, and the average node diameter was approximately 300 micrometers. In comparison to the length scale of the MFC fibers, which are on the order of tens of microns in length with larger scale tertiary structures due to fiber entanglement, as seen in Figure 12a, it is expected that the fibers are trapped within the foam liquid phase. Such two-fluid behavior is consistent with dynamics observed during micro-rheology characterization of these MFC

dispersions, where increased yield stress was observed during slow deformation of the fluid that caused local drainage (Song et al., 2019b).

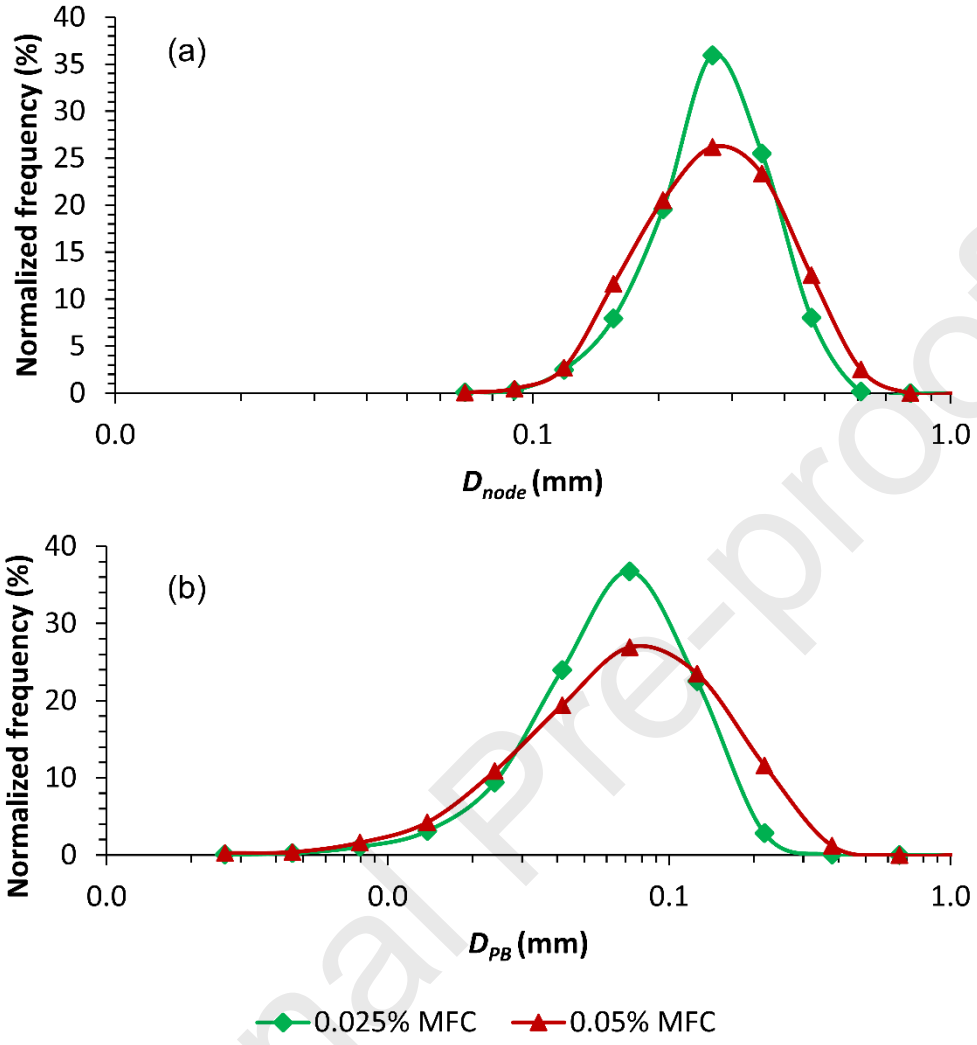

Figure 15: Normalized frequency distribution of (a) Volume equivalent diameter of nodes (D_{node}), (b) Volume equivalent diameter of Plateau borders (D_{PB}) for the MFC 0.025% and 0.05% foams aged by approximately 45 minutes obtained from pore network modeling. The average PB diameter was 73 µm and 89 µm for the 0.025% and 0.05% MFC foams.

Prior to the foam being arrested, the change in bubble size over time was evaluated to investigate how MFC influences the foam aging mechanisms of diffusive coarsening and coalescence. For both MFC concentrations, an increase in Sauter mean bubble diameter (d_{32}) and decrease in bubble count (N) were observed with respect to foam aging time. The results are provided in Table 4. For the 0.05% MFC foam, the change in bubble size was slower which was due to the lower likelihood of coalescence and slower diffusive coarsening as it was a more viscous medium. These measurements

suggest that diffusive coarsening and coalescence occurred before the foam was arrested.

Table 4: Sauter mean diameter (d_{32}) and the Total number of bubbles (N) for the 0.025% and 0.05% MFC foam at different aging times (t). Greater change in bubble size and higher reduction in number of bubbles is observed at the lower concentration of MFC which is more prone to coalescence.

MFC 0.025%	**46 mins**	**52 mins**	**58 mins**	**64 mins**
d_{32} (mm)	1.08	1.11	1.19	1.25
N	2765	2739	2250	2005
MFC 0.05%	**47 mins**	**53 mins**	**59 mins**	**65 mins**
d_{32} (mm)	0.80	0.81	0.85	0.87
N	3757	3495	3247	3162

Further evidence of diffusive coarsening was found by considering the frequency distributions of bubble sizes versus time. The 3D volume renderings in Figure 16a suggest that the foam bubbles become bigger and lesser in number with respect to foam aging time. Further details of the size distributions are provided in Figure 16b, which shows that the proportion of intermediate bubbles decreased over time while the proportion of larger bubbles grew, and the number of smaller bubbles increased. This behavior is characteristic of diffusive coarsening and aligns with findings of Lemlich (1978) which suggested that for a coarsening-only system, bubbles with radii smaller than the instantaneous radius (r_{21}) will shrink, while bubbles with radii larger than r_{21} will grow over time. While some large bubbles are possibly formed via coalescence, it is reasonable to conclude that the smaller bubbles can only form due to diffusive coarsening since the formation of satellite bubbles during coalescence in such a viscous medium was unlikely.

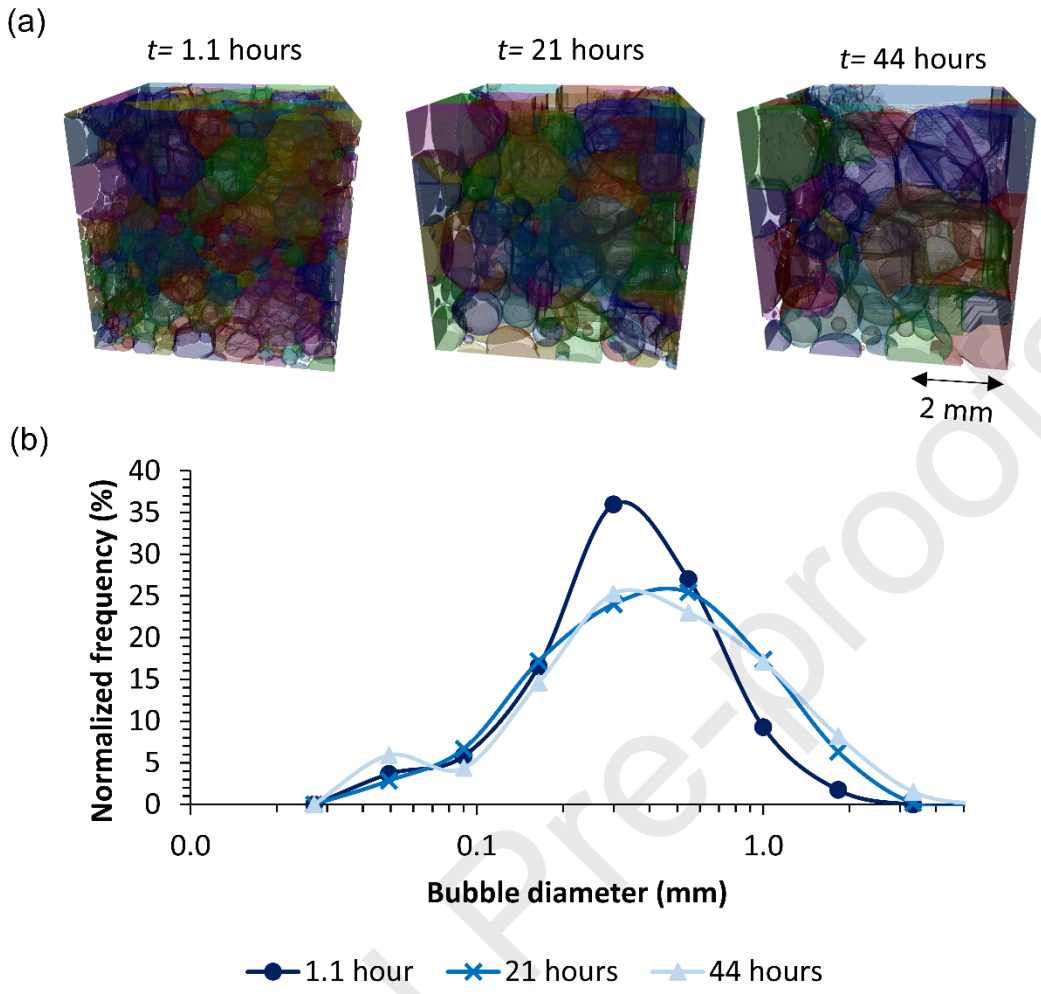

Figure 16: (a) 3D volume renderings of the 0.05% MFC foams at t= 1.1 hours, 21 hours, and 44 hours, (b) Frequency distribution of bubble sizes at these corresponding aging times showing propagation of diffusive coarsening occurring as intermediate bubbles larger than r_{21} grow, and intermediate bubbles smaller than r_{21} shrink. This causes a reduction in the number of intermediate bubbles and an increase in the number of smaller bubbles, and the number of larger bubbles leading to a bimodal size distribution.

Indeed, it is difficult to decouple coalescence and diffusive coarsening, it is reasonable to suspect that coalescence events would reduce with aging time as the effective MFC fiber concentration increases. This effect mainly relates to viscosity since it is difficult for highly viscous films to rupture and coalesce. Certainly, coalescence was observed with the 0.025% MFC foam for the first hour of aging (see Figure 9), but little or no coalescence was observed for the 0.05% MFC foam. Hence, coalescence occurs during foam generation and immediately after foam formation when the effective viscosity of the interstitial fluid remains relatively low, while diffusive coarsening appears to dominate at later times before the foam becomes arrested.

Additionally, it is reasonable to conclude that diffusive-coarsening processes dominate over the coalescence and drainage mechanisms in the post-foam arrest regime and is primarily responsible for the foam death. However, such late aging times were not covered in this study as we were more interested to test the limitations of micro-CT imaging by considering early aging times when the foam dynamics are relatively faster.

4. Conclusions

Our study focused on how MFC nanofibers impacted foam drainage, coalescence, and diffusive coarsening mechanisms at the microscopic scale. We found that the stabilization mechanism of MFC fibers is unique and differs from that of Pickering foams stabilized by inorganic particles, such as silica nanoparticles, which involve denser crowding of particles at the foam-liquid interface to achieve stabilization (Stocco et al., 2011a; Stocco et al., 2011b). The MFC nanofibers are efficient at arresting foams with only a small weight percentage of fibers (<0.05%) due to the high aspect ratio of the fibers, and their ability to form entangled tertiary structures which enhances the bulk viscosity of the interstitial fluid and restrict foam drainage. This effectiveness, at such low weight percentages, would be highly preferred for many industrial applications as it is economically viable and does not produce undesirable thick mixtures. In addition, the substitution of inorganic particles with MFC to achieve foam stabilization would be an environmentally friendly option since MFC is non-toxic and biodegradable (Abdul Khalil et al., 2012). Therefore, MFC could be applicable for a wider range of applications, such as drug delivery, food, and cosmetics where non-toxicity is a prerequisite (Guevara et al., 2013).

The main findings are the following.

(1) Dynamic micro-CT imaging coupled with EfficientU-net segmentation can provide an accurate 3D geometrical representation of dynamically aging MFC foams.
(2) The proposed technique can achieve a high temporal resolution of 6 minutes. This is extremely uncommon with bench-top micro-CT systems, which are generally considered unsuitable for studying fast-aging systems.
(3) The machine-learning segmentation approach demonstrated is transferable to low SNR data, which can in turn enhance the temporal resolution of any 3D imaging technique.
(4) A small weight percentage of MFC can be effective at significantly stabilizing liquid foams due to the entanglement and high aspect ratio of the MFC.
(5) MFC becomes trapped within the foam structure and concentrates over time, and eventually reaches a critical concentration where the foam is arrested.

(6) Employing multimodal imaging such as micro-CT, CLSM, and bulk foam imaging can provide an effective means to study microscale foam stability mechanisms as opposed to traditional bulk foam studies.

While these findings highlight the foam stabilization mechanisms of MFC, further work is required to elucidate the critical MFC concentration at which this arrest occurs. In addition, while MFC is effective at foam stabilization, the influence of its fiber length and fiber concentration on the degree of entanglement remains unclear and could be the focus of future work. Lastly, the proposed machine-learning technique coupled with micro-CT could be implemented to study a wide range of soft matter systems that are composed of immiscible phases. As such, the scope of this work lies beyond the study of only MFC; the proposed methodology could be utilized to study various phase separation processes, aging dynamics of foams, and/or the aggregation of emulsion droplets where a temporal resolution in the order of few minutes can be useful to quantify the aging dynamics.

5. CRediT author statement

SRM: Conceptualization, Methodology, Software, Validation, Formal analysis, Investigation, Data curation, Writing- original draft, Visualization **PTS:** Conceptualization, Investigation, Writing- reviewing and editing **KT:** Methodology, Software, Visualization **YN:** Software, Visualization **SMH:** Investigation **PM:** Writing- reviewing and editing **RTA:** Supervision, Conceptualization, Methodology, Validation, Funding Acquisition, Writing- reviewing and editing

6. Acknowledgments

Syeda R. Muin acknowledges the contribution of the Australian Government Research Training Program (RTP) Scholarship. The authors also acknowledge the Tyree X-ray CT Facility, a UNSW network lab funded by the UNSW Research Infrastructure Scheme, for the acquisition of the 3D µXCT images.

7. Appendix:

7.1 Calculation for theoretical free drainage time

The timescale for free drainage (t_{drain}) is estimated using the following equation (Koehler et al., 2000; Rio et al., 2014):

$$t_{drain} = \frac{H\eta}{\kappa\rho g R^2 \phi^{\alpha}}$$

where H is the average foam height of the three replicates estimated from the bulk foam images, η is the viscosity at a shear rate of 1 s^{-1}, κ is a dimensionless permeability constant of order 10^{-2}, ϕ is the liquid fraction estimated from the micro-CT image analysis, α is the mobility constant which is assumed as 0.5 in this case (Saint-Jalmes et al., 2004), g is gravitational acceleration of 9.81 ms^{-2} and ρ is assumed as density of water since presumably the fibers are retained in the foam phase, while the liquid drains out of the foam phase.

Using Equation **Error! Reference source not found.**, the estimated timescale of free drainage was 0.27 hours and 0.58 hours for the 0.025% and 0.05% MFC foams, respectively.

8. Appendix:

1. Abdul Khalil, H.P.S., Bhat, A.H., Ireana Yusra, A.F., 2012. Green composites from sustainable cellulose nanofibrils: A review. Carbohydrate Polymers 87, 963-979 DOI: https://doi.org/10.1016/j.carbpol.2011.08.078.
2. Alargova, R.G., Warhadpande, D.S., Paunov, V.N., Velev, O.D., 2004. Foam superstabilization by polymer microrods. Langmuir 20, 10371-10374 DOI: https://doi.org/10.1021/la048647a.
3. Arganda-Carreras, I., Kaynig, V., Rueden, C., Eliceiri, K.W., Schindelin, J., Cardona, A., Sebastian Seung, H., 2017. Trainable Weka Segmentation: a machine learning tool for microscopy pixel classification. Bioinformatics 33, 2424-2426 DOI: https://doi.org/10.1093/bioinformatics/btx180.
4. Armstrong, R.T., McClure, J.E., Robins, V., Liu, Z., Arns, C.H., Schlüter, S., Berg, S., 2019. Porous Media Characterization Using Minkowski Functionals: Theories, Applications and Future Directions. Transport in Porous Media 130, 305-335 DOI: https://doi.org/10.1007/s11242-018-1201-4.
5. Arriaga, L.R., Drenckhan, W., Salonen, A., Rodrigues, J.A., Iniguez-Palomares, R., Rio, E., Langevin, D., 2012. On the long-term stability of foams stabilised by mixtures of nano-particles and oppositely charged short chain surfactants. Soft Matter 8, 11085-11097 DOI: https://doi.org/10.1039/c2sm26461g.
6. Arzhavitina, A., Steckel, H., 2010. Foams for pharmaceutical and cosmetic application. International Journal of Pharmaceutics 394, 1-17 DOI: https://doi.org/10.1016/j.ijpharm.2010.04.028.
7. Barrett, J.F., Keat, N., 2004. Artifacts in CT: recognition and avoidance. Radiographics 24, 1679-1691 DOI: https://doi.org/10.1148/rg.246045065.
8. Bartsch, O.J.K.B., 1924. Beitrag zur Theorie des Schaumschwimmverfahrens. 20, 50-77.
9. Bhakta, A., Ruckenstein, E., 1997. Decay of standing foams: drainage, coalescence and collapse. Advances in Colloid and Interface Science 70, 1-124 DOI: https://doi.org/10.1016/S0001-8686(97)00031-6.
10. Boas, F.E., Fleischmann, D., 2012. CT artifacts: causes and reduction techniques. Imaging Med 4, 229-240.
11. Briceño-Ahumada, Z., Drenckhan, W., Langevin, D., 2016. Coalescence in Draining Foams Made of Very Small Bubbles. Physical Review Letters 116 DOI: https://doi.org/10.1103/PhysRevLett.116.128302.
12. Buades, A., Coll, B., Morel, J.-M., 2005. A non-local algorithm for image denoising, 2005 IEEE Computer Society Conference on Computer Vision and Pattern Recognition (CVPR'05). IEEE, pp. 60-65.
13. Buades, A., Coll, B., Morel, J.-M., 2011. Non-local means denoising. Image Processing On Line 1, 208-212 DOI: https://doi.org/10.5201/ipol.2011.bcm_nlm.
14. Bultreys, T., Boone, M.A., Boone, M.N., De Schryver, T., Masschaele, B., Van Hoorebeke, L., Cnudde, V., 2016. Fast laboratory-based micro-computed tomography for pore-scale research: Illustrative experiments and perspectives on the future. Advances in Water Resources 95, 341-351.
15. Bureiko, A., Trybala, A., Kovalchuk, N., Starov, V., 2015. Current applications of foams formed from mixed surfactant–polymer solutions. Advances in Colloid and Interface Science 222, 670-677 DOI: http://dx.doi.org/10.1016/j.cis.2014.10.001.
16. Carrier, V., Colin, A., 2003. Coalescence in Draining Foams. Langmuir 19, 4535-4538 DOI: https://doi.org/10.1021/la026995b.
17. Cervin, N.T., Johansson, E., Benjamins, J.-W., Wågberg, L., 2015. Mechanisms Behind the Stabilizing Action of Cellulose Nanofibrils in Wet-Stable Cellulose Foams. Biomacromolecules 16, 822-831 DOI: https://doi.org/10.1021/bm5017173.

18. Charreau, H., L Foresti, M., Vazquez, A., 2013. Nanocellulose patents trends: a comprehensive review on patents on cellulose nanocrystals, microfibrillated and bacterial cellulose. Recent patents on nanotechnology 7, 56-80.
19. Cheng, H.C., Lemlich, R., 1983. Errors in the measurement of bubble size distribution in foam. Industrial & engineering chemistry fundamentals 22, 105-109 DOI: https://doi.org/10.1021/i100009a018.
20. Cho, Y.S., Laskowski, J.S., 2002. Bubble coalescence and its effect on dynamic foam stability. The Canadian Journal of Chemical Engineering 80, 299-305 DOI: https://doi.org/10.1002/cjce.5450800216.
21. Clausnitzer, V., Hopmans, J.W., 1999. Determination of phase-volume fractions from tomographic measurements in two-phase systems. Advances in Water Resources 22, 577-584 DOI: https://doi.org/10.1016/S0309-1708(98)00040-2.
22. Cnudde, V., Boone, M.N., 2013. High-resolution X-ray computed tomography in geosciences: A review of the current technology and applications. Earth-Science Reviews 123, 1-17 DOI: https://doi.org/10.1016/j.earscirev.2013.04.003.
23. Da Wang, Y., Shabaninejad, M., Armstrong, R.T., Mostaghimi, P., 2020. Physical accuracy of deep neural networks for 2d and 3d multi-mineral segmentation of rock micro-CT images. arXiv preprint arXiv:2002.05322.
24. Damodaran, S., 2005. Protein stabilization of emulsions and foams. Journal of Food Science 70, R54-R66 DOI: https://doi.org/10.1111/j.1365-2621.2005.tb07150.x.
25. Di Michiel, M., Merino, J.M., Fernandez-Carreiras, D., Buslaps, T., Honkimäki, V., Falus, P., Martins, T., Svensson, O., 2005. Fast microtomography using high energy synchrotron radiation. Review of Scientific Instruments 76, 043702 DOI: https://doi.org/10.1063/1.1884194.
26. Dickinson, E., 2010. Food emulsions and foams: Stabilization by particles. Current Opinion in Colloid & Interface Science 15, 40-49 DOI: https://doi.org/10.1016/j.cocis.2009.11.001.
27. Drenckhan, W., Hutzler, S., 2015. Structure and energy of liquid foams. Advances in Colloid and Interface Science 224, 1-16 DOI: https://doi.org/10.1016/j.cis.2015.05.004.
28. Exerowa, D., Kruglyakov, P.M., 1997. Foam and foam films: theory, experiment, application. Elsevier.
29. Farrokhpay, S., 2011. The significance of froth stability in mineral flotation—A review. Advances in Colloid and Interface Science 166, 1-7 DOI: https://doi.org/10.1016/j.cis.2011.03.001.
30. Gandolfo, F.G., Rosano, H.L., 1997. Interbubble Gas Diffusion and the Stability of Foams. Journal of colloid and interface science 194, 31-36 DOI: https://doi.org/10.1006/jcis.1997.5067.
31. García-Moreno, F., Kamm, P.H., Neu, T., Heim, K., Rack, A., Banhart, J., 2017. In situ X-ray tomography of aqueous foams: Analysis of columnar foam generation. Colloids and Surfaces A: Physicochemical and Engineering Aspects 534, 78-84 DOI: https://doi.org/10.1016/j.colsurfa.2017.03.011.
32. Gonzenbach, U.T., Studart, A.R., Tervoort, E., Gauckler, L.J., 2006. Stabilization of foams with inorganic colloidal particles. Langmuir 22, 10983-10988 DOI: https://doi.org/10.1021/la061825a.
33. Graetz, J., Dombrowski, J., Eggert, A., Rack, A., Kulozik, U., Hinrichs, J., Hanke, R., Zabler, S., 2020. Synchrotron micro-CT for studying coarsening in milk protein-stabilized foams in situ. Colloids and Surfaces A: Physicochemical and Engineering Aspects 601, 124832 DOI: https://doi.org/10.1016/j.colsurfa.2020.124832.
34. Guevara, J.S., Mejia, A.F., Shuai, M., Chang, Y.-W., Mannan, M.S., Cheng, Z., 2013. Stabilization of Pickering foams by high-aspect-ratio nano-sheets. Soft Matter 9, 1327-1336 DOI: https://doi.org/10.1039/C2SM27061G

35. Hailing, P.J., Walstra, P., 1981. Protein-stabilized foams and emulsions. Critical Reviews in Food Science & Nutrition 15, 155-203 DOI: https://doi.org/10.1080/10408398109527315.
36. He, K., Zhang, X., Ren, S., Sun, J., 2016. Deep residual learning for image recognition, Proceedings of the IEEE conference on computer vision and pattern recognition, pp. 770-778.
37. Hilgenfeldt, S., Koehler, S.A., Stone, H.A., 2001. Dynamics of coarsening foams: Accelerated and self-limiting drainage. Physical Review Letters 86, 4704-4707 DOI: https://doi.org/10.1103/PhysRevLett.86.4704.
38. Hill, R.J., 2008. Elastic Modulus of Microfibrillar Cellulose Gels. Biomacromolecules 9, 2963-2966 DOI: https://doi.org/10.1021/bm800490x.
39. Hunter, T.N., Wanless, E.J., Jameson, G.J., Pugh, R.J., 2009. Non-ionic surfactant interactions with hydrophobic nanoparticles: Impact on foam stability. Colloids and Surfaces A: Physicochemical and Engineering Aspects 347, 81-89 DOI: https://doi.org/10.1016/j.colsurfa.2008.12.027.
40. Hutzler, S., Weaire, D., 2000. Foam coarsening under forced drainage. Philosophical Magazine Letters 80, 419-425 DOI: https://doi.org/10.1080/095008300403567.
41. Iotti, M., Gregersen, Ø.W., Moe, S., Lenes, M., 2011. Rheological Studies of Microfibrillar Cellulose Water Dispersions. Journal of Polymers and the Environment 19, 137-145 DOI: 10.1007/s10924-010-0248-2.
42. Jiang, H., Sun, D., Jampani, V., Yang, M.H., Learned-Miller, E., Kautz, J., 2018. Super SloMo: High Quality Estimation of Multiple Intermediate Frames for Video Interpolation, Proceedings of the IEEE Computer Society Conference on Computer Vision and Pattern Recognition, pp. 9000-9008.
43. Karppinen, A., Saarinen, T., Salmela, J., Laukkanen, A., Nuopponen, M., Seppälä, J., 2012. Flocculation of microfibrillated cellulose in shear flow. Cellulose 19, 1807-1819 DOI: https://doi.org/10.1007/s10570-012-9766-5.
44. Koehler, S.A., Hilgenfeldt, S., Stone, H.A., 2000. A Generalized View of Foam Drainage: Experiment and Theory. Langmuir 16, 6327-6341 DOI: https://doi.org/10.1021/la9913147.
45. Kontturi, E., Laaksonen, P., Linder, M.B., Nonappa, Gröschel, A.H., Rojas, O.J., Ikkala, O., 2018. Advanced Materials through Assembly of Nanocelluloses. Advanced Materials 30 DOI: https://doi.org/10.1002/adma.201703779.
46. Kraynik, A.M., Reinelt, D.A., van Swol, F., 2004. Structure of random foam. Physical Review Letters 93, 208301 DOI: https://doi.org/10.1103/PhysRevLett.93.208301.
47. Kruglyakov, P.M., Karakashev, S.I., Nguyen, A.V., Vilkova, N.G., 2008. Foam drainage. Current Opinion in Colloid & Interface Science 13, 163-170 DOI: https://doi.org/10.1016/j.cocis.2007.11.003.
48. Lam, S., Velikov, K.P., Velev, O.D., 2014. Pickering stabilization of foams and emulsions with particles of biological origin. Current Opinion in Colloid & Interface Science 19, 490-500 DOI: https://doi.org/10.1016/j.cocis.2014.07.003.
49. Lambert, J., Cantat, I., Delannay, R., Renault, A., Graner, F., Glazier, J.A., Veretennikov, I., Cloetens, P., 2005. Extraction of relevant physical parameters from 3D images of foams obtained by X-ray tomography. Colloids and Surfaces A: Physicochemical and Engineering Aspects 263, 295-302 DOI: https://doi.org/10.1016/j.colsurfa.2005.01.002.
50. Langevin, D., 2015. Bubble coalescence in pure liquids and in surfactant solutions. Current Opinion in Colloid and Interface Science 20, 92-97 DOI: https://doi.org/10.1016/j.cocis.2015.03.005.
51. Lavoine, N., Bergström, L., 2017. Nanocellulose-based foams and aerogels: processing, properties, and applications. Journal of Materials Chemistry A 5, 16105-16117 DOI: https://doi.org/10.1039/C7TA02807E

52. Lemlich, R., 1978. Prediction of Changes in Bubble Size Distribution Due to Interbubble Gas Diffusion in Foam. Industrial and Engineering Chemistry Fundamentals 17, 89-93 DOI: https://doi.org/10.1021/i160066a003.
53. Magrabi, S., Dlugogorski, B., Jameson, G., 2001. Free drainage in aqueous foams: model and experimental study. AIChE Journal 47, 314-327 DOI: https://doi.org/10.1002/aic.690470210.
54. Manjón, J.V., Carbonell-Caballero, J., Lull, J.J., García-Martí, G., Martí-Bonmatí, L., Robles, M., 2008. MRI denoising using non-local means. Medical image analysis 12, 514-523 DOI: https://doi.org/10.1016/j.media.2008.02.004.
55. Martoïa, F., Dumont, P., Orgéas, L., Belgacem, M., Putaux, J.-L., 2016. Micro-mechanics of electrostatically stabilized suspensions of cellulose nanofibrils under steady state shear flow. Soft Matter 12, 1721-1735 DOI: https://doi.org/10.1039/C5SM02310F
56. Matis, K.A., Mavros, P., 1991. Foam/Froth Flotation. Separation and Purification Methods 20, 163-198 DOI: https://doi.org/10.1080/03602549108021414
57. Meagher, A., Mukherjee, M., Weaire, D., Hutzler, S., Banhart, J., Garcia-Moreno, F., 2011. Analysis of the internal structure of monodisperse liquid foams by X-ray tomography. Soft Matter 7, 9881-9885 DOI: https://doi.org/10.1039/C1SM05495C.
58. Mendoza, L., Gunawardhana, T., Batchelor, W., Garnier, G., 2018. Effects of fibre dimension and charge density on nanocellulose gels. Journal of colloid and interface science 525, 119-125 DOI: https://doi.org/10.1016/j.jcis.2018.04.077.
59. Michielsen, K., De Raedt, H., 2001. Integral-geometry morphological image analysis. Physics Reports 347, 461-538 DOI: https://doi.org/10.1016/S0370-1573(00)00106-X.
60. Muin, S.R., Rabbani, A., Bournival, G., Ata, S., Armstrong, R.T., 2020. Utilization of microcomputed tomography and pore network modeling to characterize foam dynamics. Chemical Engineering Science 230, 116174 DOI: https://doi.org/10.1016/j.ces.2020.116174.
61. Nakagaito, A.N., Fujimura, A., Sakai, T., Hama, Y., Yano, H., 2009. Production of microfibrillated cellulose (MFC)-reinforced polylactic acid (PLA) nanocomposites from sheets obtained by a papermaking-like process. Composites Science and Technology 69, 1293-1297 DOI: https://doi.org/10.1016/j.compscitech.2009.03.004.
62. Neethling, S., Lee, H., Grassia, P., 2005. The growth, drainage and breakdown of foams. Colloids and Surfaces A: Physicochemical and Engineering Aspects 263, 184-196 DOI: https://doi.org/10.1016/j.colsurfa.2004.12.014.
63. Niu, Y., Mostaghimi, P., Shabaninejad, M., Swietojanski, P., Armstrong, R.T., 2020. Digital rock segmentation for petrophysical analysis with reduced user bias using convolutional neural networks. Water Resources Research 56, e2019WR026597 DOI: https://doi.org/10.1029/2019WR026597.
64. Ohser, J., Mücklich, F., 2000. Statistical analysis of microstructures in materials science. Wiley.
65. Pääkkö, M., Ankerfors, M., Kosonen, H., Nykänen, A., Ahola, S., Österberg, M., Ruokolainen, J., Laine, J., Larsson, P.T., Ikkala, O., 2007. Enzymatic hydrolysis combined with mechanical shearing and high-pressure homogenization for nanoscale cellulose fibrils and strong gels. Biomacromolecules 8, 1934-1941 DOI: https://doi.org/10.1021/bm061215p.
66. Papara, M., Zabulis, X., Karapantsios, T.D., 2009. Container effects on the free drainage of wet foams. Chemical Engineering Science 64, 1404-1415 DOI: https://doi.org/10.1016/j.ces.2008.11.021.
67. Park, H.S., Chung, Y.E., Seo, J.K., 2015. Computed tomographic beam-hardening artefacts: mathematical characterization and analysis. Philosophical Transactions of the Royal Society A: Mathematical, Physical and Engineering Sciences 373, 20140388 DOI: https://doi.org/10.1098/rsta.2014.0388.
68. Pitois, O., Fritz, C., Vignes-Adler, M., 2005. Liquid drainage through aqueous foam: study of the flow on the bubble scale. Journal of colloid and interface science 282, 458-465 DOI: https://doi.org/10.1016/j.jcis.2004.08.187.

69. Pugh, R., 1996. Foaming, foam films, antifoaming and defoaming. Advances in Colloid and Interface Science 64, 67-142 DOI: https://doi.org/10.1016/0001-8686(95)00280-4.
70. Rio, E., Drenckhan, W., Salonen, A., Langevin, D., 2014. Unusually stable liquid foams. Advances in Colloid and Interface Science 205, 74-86 DOI: https://doi.org/10.1016/j.cis.2013.10.023.
71. Ritman, E.L., 2011. Current status of developments and applications of micro-CT. Annual review of biomedical engineering 13, 531-552 DOI: https://doi.org/10.1146/annurev-bioeng-071910-124717.
72. Ronneberger, O., Fischer, P., Brox, T., 2015. U-net: Convolutional networks for biomedical image segmentation, International Conference on Medical image computing and computer-assisted intervention. Springer, pp. 234-241.
73. Rossen, W.R., 2017. Foams in enhanced oil recovery, Foams: Theory, Measurements and Applications, pp. 413-464.
74. Saarikoski, E., Saarinen, T., Salmela, J., Seppälä, J., 2012. Flocculated flow of microfibrillated cellulose water suspensions: an imaging approach for characterisation of rheological behaviour. Cellulose 19, 647-659 DOI: https://doi.org/10.1007/s10570-012-9661-0.
75. Safouane, M., Saint-Jalmes, A., Bergeron, V., Langevin, D.J.T.E.P.J.E., 2006. Viscosity effects in foam drainage:Newtonian and non-newtonian foaming fluids. 19, 195-202 DOI: https://doi.org/10.1140/epje/e2006-00025-4.
76. Saint-Jalmes, A., 2006. Physical chemistry in foam drainage and coarsening. Soft Matter 2, 836-849 DOI: https://doi.org/10.1039/B606780H.
77. Saint-Jalmes, A., Zhang, Y., Langevin, D., 2004. Quantitative description of foam drainage: Transitions with surface mobility. European Physical Journal E 15, 53-60 DOI: https://doi.org/10.1140/epje/i2004-10036-x.
78. Sarker, S., Chowdhury, S., Laha, S., Dey, D., 2012. Use of non-local means filter to denoise image corrupted by salt and pepper noise. Signal & Image Processing 3, 223.
79. Schindelin, J., Arganda-Carreras, I., Frise, E., Kaynig, V., Longair, M., Pietzsch, T., Preibisch, S., Rueden, C., Saalfeld, S., Schmid, B., 2012. Fiji: an open-source platform for biological-image analysis. Nature methods 9, 676-682 DOI: https://doi.org/10.1038/nmeth.2019.
80. Schlüter, S., Sheppard, A., Brown, K., Wildenschild, D., 2014. Image processing of multiphase images obtained via X-ray microtomography: a review. Water Resources Research 50, 3615-3639 DOI: https://doi.org/10.1002/2014WR015256.
81. Schoeman, L., Williams, P., du Plessis, A., Manley, M., 2016. X-ray micro-computed tomography (μCT) for non-destructive characterisation of food microstructure. Trends in Food Science & Technology 47, 10-24 DOI: https://doi.org/10.1016/j.tifs.2015.10.016.
82. Shelhamer, E., Long, J., Darrell, T., 2017. Fully Convolutional Networks for Semantic Segmentation. IEEE Transactions on Pattern Analysis and Machine Intelligence 39, 640-651 DOI: https://doi.org/10.1109/TPAMI.2016.2572683.
83. Sheppard, A.P., Sok, R.M., Averdunk, H., 2004. Techniques for image enhancement and segmentation of tomographic images of porous materials. Physica A: Statistical Mechanics and its Applications 339, 145-151 DOI: https://doi.org/10.1016/j.physa.2004.03.057.
84. Solomon, M.J., Spicer, P.T., 2010. Microstructural regimes of colloidal rod suspensions, gels, and glasses. Soft Matter 6, 1391-1400 DOI: https://doi.org/10.1039/B918281K.
85. Song, J., Caggioni, M., Squires, T.M., Gilchrist, J.F., Prescott, S.W., Spicer, P.T., 2019a. Heterogeneity, suspension, and yielding in sparse microfibrous cellulose gels 1. Bubble rheometer studies. Rheologica Acta 58, 217-229 DOI: https://doi.org/10.1007/s00397-019-01140-4.
86. Song, J., Caggioni, M., Squires, T.M., Gilchrist, J.F., Prescott, S.W., Spicer, P.T., 2019b. Heterogeneity, suspension, and yielding in sparse microfibrous cellulose gels 2: strain rate-dependent two-fluid behavior. Rheologica Acta 58, 231-239 DOI: https://doi.org/10.1007/s00397-019-01141-3.

87. Stevenson, P., 2010. Inter-bubble gas diffusion in liquid foam. Current Opinion in Colloid & Interface Science 15, 374-381 DOI: https://doi.org/10.1016/j.cocis.2010.05.010.
88. Stocco, A., Garcia-Moreno, F., Manke, I., Banhart, J., Langevin, D., 2011a. Particle-stabilised foams: structure and aging. Soft Matter 7, 631-637 DOI: https://doi.org/10.1039/C0SM00166J.
89. Stocco, A., Rio, E., Binks, B.P., Langevin, D., 2011b. Aqueous foams stabilized solely by particles. Soft Matter 7, 1260-1267 DOI: https://doi.org/10.1039/C0SM01290D.
90. Stone, H., Koehler, S., Hilgenfeldt, S., Durand, M., 2002. Perspectives on foam drainage and the influence of interfacial rheology. Journal of Physics: Condensed Matter 15, S283 DOI: https://doi.org/10.1088/0953-8984/15/1/338.
91. Swain, M.V., Xue, J., 2009. State of the art of Micro-CT applications in dental research. International journal of oral science 1, 177-188 DOI: https://doi.org/10.4248/IJOS09031.
92. Tamada, D., Kromrey, M.L., Ichikawa, S., Onishi, H., Motosugi, U., 2020. Motion artifact reduction using a convolutional neural network for dynamic contrast enhanced mr imaging of the liver. Magnetic Resonance in Medical Sciences 19, 64-76 DOI: https://doi.org/10.2463/mrms.mp.2018-0156.
93. Tan, M., Le, Q., 2019. Efficientnet: Rethinking model scaling for convolutional neural networks, International Conference on Machine Learning. PMLR, pp. 6105-6114.
94. Tatsumi, D., Ishioka, S., Matsumoto, T., 2002. Effect of fiber concentration and axial ratio on the rheological properties of cellulose fiber suspensions. Nihon Reoroji Gakkaishi 30, 27-32 DOI: https://doi.org/10.1678/rheology.30.27.
95. Verbist, G., Weaire, D., Kraynik, A.M., 1996. The foam drainage equation. Journal of Physics Condensed Matter 8, 3715-3731 DOI: https://doi.org/10.1088/0953-8984/8/21/002.
96. Vincent, L., Soille, P., 1991. Watersheds in digital spaces: an efficient algorithm based on immersion simulations. IEEE Computer Architecture Letters 13, 583-598.
97. Wang, Y., Miller, J., 2020. Current developments and applications of micro-CT for the 3D analysis of multiphase mineral systems in geometallurgy. Earth-Science Reviews, 103406.
98. Wang, Y.D., Blunt, M.J., Armstrong, R.T., Mostaghimi, P., 2021. Deep learning in pore scale imaging and modeling. Earth-Science Reviews 215, 103555 DOI: https://doi.org/10.1016/j.earscirev.2021.103555.
99. Weaire, D.L., Hutzler, S., 2001. The Physics of Foams. Oxford University Press.
100. Wildenschild, D., Sheppard, A.P., 2013. X-ray imaging and analysis techniques for quantifying pore-scale structure and processes in subsurface porous medium systems. Advances in Water Resources 51, 217-246 DOI: https://doi.org/10.1016/j.advwatres.2012.07.018.
101. Xiang, L., Chen, Y., Chang, W., Zhan, Y., Lin, W., Wang, Q., Shen, D., 2019a. Deep-Learning-Based Multi-Modal Fusion for Fast MR Reconstruction. IEEE Transactions on Biomedical Engineering 66, 2105-2114 DOI: https://doi.org/10.1109/TBME.2018.2883958.
102. Xiang, W., Preisig, N., Ketola, A., Tardy, B.L., Bai, L., Ketoja, J.A., Stubenrauch, C., Rojas, O.J., 2019b. How Cellulose Nanofibrils Affect Bulk, Surface, and Foam Properties of Anionic Surfactant Solutions. Biomacromolecules 20, 4361-4369 DOI: https://doi.org/10.1021/acs.biomac.9b01037.

Declaration of interests

☒ The authors declare that they have no known competing financial interests or personal relationships that could have appeared to influence the work reported in this paper.

☐The authors declare the following financial interests/personal relationships which may be considered as potential competing interests:

Highlights

- Trapping of micro-cellulose and entanglement of fibres within the foam structure results in an arrested foam.
- Deep learning allows for quantitative 3D morphological analyses of liquid foams imaged with X-ray microtomography.
- 3D microstructural analyses elucidates the time evolution of foam Plateau borders and nodes under dynamic conditions.